















## MAGAZ3NE: Spatially Resolved Ages and Chemical Abundances of Ultra-Massive Quiescent Galaxies at $z \sim 3.5$ using JWST/NIRSpec IFU

ADIT H. EDWARD <sup>1</sup>, JACQUELINE ANTWI-DANSO <sup>2,3,4,\*</sup>, ADAM MUZZIN <sup>1</sup>, BEN FORREST <sup>5</sup>, IAN MCCONACHIE <sup>6</sup>,  
ALIZA BEVERAGE <sup>7,8,†</sup>, WENJUN CHANG <sup>9</sup>, M. C. COOPER <sup>10</sup>, PERCY GOMEZ<sup>11</sup>, MASSISSILIA L. HAMADOUCHE <sup>4</sup>,  
AURÉLIEN HENRY <sup>12</sup>, HAN LEI <sup>13</sup>, DANILO MARCHESINI <sup>14</sup>, ALLISON NOBLE<sup>15,16</sup>, STEPHANIE M. URBANO STAWINSKI<sup>17</sup>,  
GILLIAN WILSON <sup>12</sup> AND M. E. WISZ <sup>12</sup>

<sup>1</sup>*Department of Physics and Astronomy, York University, 4700 Keele St. Toronto, Ontario, M3J 1P3, Canada*

<sup>2</sup>*David A. Dunlap Department of Astronomy and Astrophysics, University of Toronto, 50 St. George Street, Toronto, Ontario, M5S 3H4, Canada*

<sup>3</sup>*Dunlap Institute for Astronomy & Astrophysics, University of Toronto, 50 St George Street, Toronto, ON M5S 3H4, Canada*

<sup>4</sup>*Department of Astronomy, University of Massachusetts, Amherst, MA 01003, USA*

<sup>5</sup>*Department of Physics and Astronomy, University of California Davis, One Shields Avenue, Davis, CA, 95616, USA*

<sup>6</sup>*Department of Astronomy, University of Wisconsin-Madison, 475 N. Charter St., Madison, WI 53706 USA*

<sup>7</sup>*Observatories of the Carnegie Institution for Science, 813 Santa Barbara Street, Pasadena, CA 91101, USA*

<sup>8</sup>*Department of Astrophysical Sciences, Princeton University, 4 Ivy Lane, Princeton, NJ 08544, USA*

<sup>9</sup>*Department of Physics and Astronomy, University of California, Riverside, 900 University Avenue, Riverside, CA 92521, USA*

<sup>10</sup>*Center for Cosmology, Department of Physics and Astronomy, University of California, Irvine, Irvine, CA, USA*

<sup>11</sup>*W.M. Keck Observatory, 65-1120 Mamalahoa Hwy., Kamuela, HI 96743, USA*

<sup>12</sup>*Department of Physics, University of California, Merced, 5200 Lake Road, Merced, CA 95343, USA*

<sup>13</sup>*Department of Physics, McGill Space Institute, McGill University, 3600 rue University, Montréal, Québec H3A 2T8, Canada*

<sup>14</sup>*Department of Physics & Astronomy, Tufts University, MA 02155, USA*

<sup>15</sup>*School of Earth and Space Exploration, Arizona State University, Tempe, AZ 85287, USA*

<sup>16</sup>*Beus Center for Cosmic Foundations, Arizona State University, Tempe, AZ 85287 USA*

<sup>17</sup>*Department of Physics, University of California, Santa Barbara, Santa Barbara, CA 93106, USA*

### ABSTRACT

We present spatially-resolved measurements of stellar age,  $[\text{Fe}/\text{H}]$ , and  $[\alpha/\text{Fe}]$  in three ultra-massive ( $\log(M_*/M_\odot) > 11$ ), compact ( $R_e \lesssim 2$  kpc) quiescent galaxies at  $z \sim 3.5$  using JWST/NIRSpec IFU spectroscopy. These observations provide the first spatially-resolved constraints on  $\alpha$ -enhancement at this epoch, enabling a direct test of quenching mechanisms before late-time assembly processes such as mergers can erase chemical signatures. The central regions of all three galaxies show both uniformly young ages ( $\approx 0.6 - 0.7$  Gyr) and elevated  $[\alpha/\text{Fe}]$  ( $\approx 0.2 - 0.5$ ), indicating rapid, enhanced star formation shortly before recent quenching. Beyond the cores, two galaxies display positive age gradients and negative  $[\alpha/\text{Fe}]$  gradients, consistent with rapid merger-driven quenching, while the third shows a flat age profile indicative of uniform quenching. The  $[\text{Fe}/\text{H}]$  gradients are also consistent with these trends, though we note that the metallicities reported by codes using  $\alpha$ -enhanced models differ significantly ( $\approx 0.2 - 0.4$  dex) from those reported using solar-scaled templates. These data demonstrate that quenching pathways are diverse by  $z \sim 3.5$ , with rapid, merger-driven quenching already operating in a subset of massive quiescent galaxies in the first two billion years of cosmic time. Furthermore, these results establish that explicit treatment of  $\alpha$ -enhancement is essential for interpreting the star-formation histories of the earliest quenched systems.

**Keywords:** Galaxies (573) — Galactic Abundances (2002) — High-Redshift Galaxies (734) — Galaxy Evolution (594) — Galaxy Quenching (2040) — Galaxy Formation (595)

## 1. INTRODUCTION

Since the first discoveries of massive quiescent galaxies (MQGs) in the early Universe (e.g., J. Dunlop et al. 1996; K. Glazebrook et al. 2004; E. Daddi et al. 2005; M. Kriek et al. 2006, 2008, 2009), they have remained one of the most active areas of research in the following decades (e.g., P. G. van Dokkum et al. 2008; R. Bezanson et al. 2009; D. Marchesini et al. 2010; A. B. Newman et al. 2010; G. B. Brammer et al. 2011; A. W. S. Man et al. 2012; A. Muzzin et al. 2012; J. van de Sande et al. 2013; K. E. Whitaker et al. 2013; C. M. S. Straatman et al. 2014; S. Belli et al. 2014, 2015; A. B. Newman et al. 2015; M. Kriek et al. 2016; K. Glazebrook et al. 2017; Z. C. Marsan et al. 2017; S. Belli et al. 2017; A. B. Newman et al. 2018; M. Kriek et al. 2019; S. Belli et al. 2019; M. Kriek et al. 2019; M. Akhshik et al. 2020; M. Jafariyazani et al. 2020; B. Forrest et al. 2020a, 2022; M. Akhshik et al. 2023; S. M. Urbano Stawinski et al. 2024; K. Ito et al. 2025; J. Antwi-Danso et al. 2025; M. Jafariyazani et al. 2025).

The James Webb Space Telescope (JWST) has already advanced this field significantly, identifying MQGs at earlier times than was possible with ground-based telescopes (e.g., A. C. Carnall et al. 2023a,b, 2024; A. Weibel et al. 2025; T. Nanayakkara et al. 2024; F. D’Eugenio et al. 2024; L. Wright et al. 2024; W. M. Baker et al. 2025; A. de Graaff et al. 2025; T. Yang et al. 2026; M. L. Hamadouche et al. 2026b; Z. Ji et al. 2026; Y. Zhang et al. 2026a). In particular, high signal-to-noise JWST spectroscopy has enabled more precise star formation history (SFH) modeling, improving insights into past star-formation and quenching (e.g., M. Park et al. 2024; K. Glazebrook et al. 2024; A. G. Beverage et al. 2024, 2025; C. M. Cheng et al. 2025; I. McConachie et al. 2025a; M. L. Hamadouche et al. 2026b; K. Lisiecki et al. 2026; Y. Zhang et al. 2026b). However, JWST observations of early MQGs have heightened previous tensions between observations and theoretical galaxy formation models for these extreme objects. Their inferred SFHs indicate earlier and more rapid formation than what is expected from both semi-analytic models and hydrodynamical simulations (i.e., C. Schreiber et al. 2018; K. Glazebrook et al. 2024; T. Nanayakkara et al. 2024; A. de Graaff et al. 2025). Resolving this tension requires improved constraints on their formation timescales, as well as a clearer understanding of the

physical mechanisms that quenched them at such early times.

In contrast to high-redshift work, the quenching histories of massive quiescent galaxies in the local Universe have been well-characterized. From these works, we have identified three broad quenching pathways: uniform, outside-in, and inside-out. In uniform quenching, the entire galaxy is quenched by the same mechanism on very short timescales of  $\lesssim 100$  Myr (D. J. Setton et al. 2020; F. D’Eugenio et al. 2024), usually presumed from active galactic nuclei (AGN) feedback. Post-starburst (PSB) galaxies at  $z \sim 0.6$  have shown this to be a dominant quenching mechanism (D. J. Setton et al. 2020). In the outside-in scenario, the galaxy quenches its star formation in the outskirts before the cores, typically from environmental effects such as tidal interactions (e.g., A. L. Schaefer et al. 2017). This leaves the stellar populations on the outskirts older than those in the central regions. Finally, inside-out quenching describes the process whereby galaxies quench their inner regions first, leaving the stellar populations in the core older than those on the periphery. On average, the cores of galaxies build up their mass earlier than their outskirts (R. García-Benito et al. 2017), independent of Hubble type, surface density, and stellar mass. Many local ellipticals are predicted to have formed through this process, due to the numerous mergers and accretions they experienced in the past (e.g. E. J. Nelson et al. 2016; L. Oldham et al. 2017; D. Zewdie et al. 2020; B. McDonough et al. 2025; M. Pizzardo et al. 2026; C. Lawlor-Forsyth et al. 2026).

Simulations provide a fourth pathway for high- $z$  galaxies: rapid, merger-driven quenching (D. Pathak et al. 2021; L. C. Kimmig et al. 2025; Y. Ni et al. 2025). In this scenario, galaxies undergo a compaction event where the gas funnels into the center of the galaxy, triggering an intense central starburst. As the gas reservoir depletes, AGN feedback suppresses further star formation, quenching the galaxy in an inside-out manner. This process occurs rapidly, quenching on timescales of  $\lesssim 200$  Myr, often following a major merger. Despite the inside-out sequence of quenching, it produces younger light-weighted cores due to the recent starburst (D. Pathak et al. 2021; Y. Ni et al. 2025).

Discerning between these different quenching pathways at high redshift requires spatially resolved measurements of age, metallicity, and  $\alpha$ -enhancement. In particular,  $\alpha$ -enhancement is an important tracer of formation histories. The  $\alpha$  elements (i.e., C, O, Ne, Mg, Si, S, Ar, Ca, Ti) are typically produced in massive stars before being released by core-collapse supernovae (SNe II) that enrich the interstellar medium (ISM) on short

Corresponding author: Adit H. Edward

Email: ahedward@yorku.ca

\* Dunlap Fellow

† NHFP Hubble Fellow

( $\lesssim 30$  Myr; A. Pipino & F. Matteucci 2009) timescales. This is in contrast to Fe-peak elements, which are produced in equal amounts by both SNe II and Type Ia supernovae (SNe Ia), although the latter occurs on much longer timescales of  $\sim 0.5 - 1$  Gyr (D. Maoz & A. Gal-Yam 2004; D. Maoz et al. 2010; C. Kobayashi & K. Nomoto 2009). It follows then that the abundance ratio  $[\alpha/\text{Fe}]$ <sup>18</sup> is a *direct* tracer of the formation timescales of young ( $< 1$  Gyr old) galaxies. A. G. Beverage et al. (2025) for instance show that star-formation timescales inferred with variable abundances are shorter than those that assume solar-scaled ( $[\alpha/\text{Fe}] = 0$ ) abundances.

The combination of age, metallicity, and  $[\alpha/\text{Fe}]$  gradients encodes information on the various quenching pathways for quiescent galaxies (R. Maiolino & F. Mannucci 2019). Measuring these gradients was difficult in the pre-JWST era, due to the high spatial and spectral resolution required, necessitating long exposure times. Deep spectroscopic surveys were therefore essential to characterize these trends statistically. C. M. Cheng et al. (2024) presented age,  $[\text{Fe}/\text{H}]$ , and  $[\text{Mg}/\text{Fe}]$  radial gradients for 456 massive quiescent galaxies at  $0.6 \lesssim z \lesssim 1.0$  from the Large Early Galaxy Astrophysics Census (LEGA-C; A. van der Wel et al. 2016, 2021; C. M. S. Straatman et al. 2018), finding flat age and  $[\text{Mg}/\text{Fe}]$  gradients, as well as negative  $[\text{Fe}/\text{H}]$  gradients. They also found that younger ( $1 \leq \text{age}/\text{Gyr} < 2.63$ ) quiescent galaxies have negative  $[\text{Fe}/\text{H}]$  and positive age gradients, consistent with a central merger-driven starburst, although minor mergers and progenitor bias (P. G. van Dokkum & M. Franx 2001; S. Belli et al. 2015; S. K. Keating et al. 2015) can produce similar signatures. Follow-up work from the JWST-Spectroscopic Ultra-deep Survey Probing Extragalactic Near-infrared Stellar Emission (SUSPENSE; M. Slob et al. 2024) studied eight massive ( $10.3 \lesssim \log(M_*/M_\odot) \lesssim 11.1$ ) quiescent galaxies at  $1.2 \lesssim z \lesssim 2.2$  (C. M. Cheng et al. 2025). They found negative age gradients, positive  $[\text{Mg}/\text{Fe}]$  gradients, and flat  $[\text{Fe}/\text{H}]$  gradients, pointing to inside-out quenching.

In contrast, very few constraints on quenching pathways exist at higher redshifts ( $z \gtrsim 2$ ). The few studies that have measured resolved stellar population parameters reveal a diverse picture. For example, P. G. Pérez-González et al. (2025) found negative  $[\text{Fe}/\text{H}]$  gradients, along with evidence of inside-out formation and high  $[\text{Mg}/\text{Fe}]$  abundances in Jekyll, a well-studied massive quiescent galaxy at  $z \sim 3.7$  (C. Schreiber et al. 2018; K. Glazebrook et al. 2024; T. Nanayakkara et al.

2024). K. Takahashi et al. (2025), on the other hand, found that the line-emitting region (a tracer of on-going star-formation) for a “mini-quenched” (e.g., T. J. Looser et al. 2024) galaxy at  $z \sim 5$  was more compact than the continuum region (a tracer of stellar mass), implying outside-in quenching. F. D’Eugenio et al. (2024) found flat age evolution in a young ( $\sim 0.5$  Gyr), massive ( $\log(M_*/M_\odot) \approx 11.2$ ), PSB at  $z \sim 3$ , which they show is most likely due to AGN feedback from the central supermassive black hole. Understanding the relative role of these different quenching processes requires deep, spatially resolved observations of their stellar light at early cosmic times, prior to late-time assembly.

To this end, we present the first spatially resolved measurements of  $[\alpha/\text{Fe}]$  for three massive ( $\log(M_*/M_\odot) > 11$ ) quiescent galaxies at  $z > 3$  using JWST NIRSpec Integral Field Unit (IFU) medium grating ( $R \sim 1000$ ) observations. With its high spatial resolution (spaxel size of  $0.1''$ ; T. Böker et al. 2022), the IFU also enables age,  $[\text{Fe}/\text{H}]$ , and SFH gradients. We can therefore obtain a more complete picture of the rapid evolution of these extreme objects. These observations allow us to directly test quenching pathways in the first 2 Gyr. The paper is structured as follows. In §2, we present the observations. In §3 and §4, we discuss our SED fitting methods and results. Finally, in §5 we discuss the implications for massive galaxy formation at high redshift. We summarize our main conclusions in §6. Throughout, we assume a P. Kroupa & C. M. Boily (2002) Initial Mass Function (IMF) and assume a flat  $\Lambda$ CDM cosmology, i.e.,  $H_0 = 70 \text{ km s}^{-1} \text{ Mpc}^{-1}$ ,  $\Omega_M = 0.3$ , and  $\Omega_\Lambda = 0.7$ .

## 2. DATA

### 2.1. JWST GO 2913

Our targets are three bright ( $K_s < 21.7$ ) massive ( $\log(M_*/M_\odot) > 11$ ) quiescent galaxies (MQGs) from the Massive Ancient Galaxies At  $z > 3$  NEar-infrared (MAGAZ3NE) Survey (B. Forrest et al. 2020b, 2024). MAGAZ3NE targets were photometrically identified from the UltraVISTA (A. Muzzin et al. 2013) and XMM-VIDEO (Annunziatella et al. in prep) catalogs and spectroscopically confirmed with Keck/MOSFIRE. Further spectroscopic follow-up with both Keck/MOSFIRE and Keck/NIRES revealed large ( $\sigma_* \gtrsim 379 \text{ km/s}$ ) velocity dispersions (B. Forrest et al. 2022). All three MQGs have subsequently had deep follow-up ALMA Band 7 observations targeting the dust-continuum (W. Chang et al. 2026). Two of the three were undetected, and only a faint detection was observed for the third (XMM-VID3-2457), confirming their quiescent nature against the possibility of dust obscured star-formation.

<sup>18</sup>  $[\text{A}/\text{B}] = \log(n(\text{A})/n(\text{B}))_* - \log(n(\text{A})/n(\text{B}))_\odot$ , where  $n(\text{X})$  is the number density of element X.

In this work, we utilize data from a JWST Cycle 2 program (ID: GO 2913; ‘Dissecting the Monsters: Resolved IFU Spectroscopy of the Most Massive Quiescent Galaxies at  $z > 3$ ’, B. Forrest et al. 2023). This program obtained JWST/NIRSpec Integral Field Unit (IFU) observations using the G235M/F170LP grating-filter configuration, which covers  $1.66 < \lambda_{\text{obs}}/\mu\text{m} < 3.17$ . At  $3.45 < z < 3.5$ , this corresponds to  $\sim 0.37 < \lambda_{\text{rest}}/\mu\text{m} < 0.70$ , capturing important rest-frame optical features sensitive to age (e.g., the Balmer series &  $D_n4000$ ), metallicity (e.g., Fe5270 & Fe5335) and  $\alpha$ -enhancement (e.g., Mgb, Ca I) (M. L. Hamadouche et al. 2026a). The IFU spaxel size of  $0.1''$  is equivalent to  $\approx 730\text{pc}$  at  $z \sim 3.5$  (B. Forrest et al. 2026), enabling spatially resolved analyses of these MQGs.

We use the same data reduction as B. Forrest et al. (2026), which first presented these data. To summarize, data reduction was initially performed with the JWST pipeline (H. Bushouse et al. 2025). To mask contaminating flux, cosmic rays and hot pixels, we flag pixels that are  $> 2\sigma_{\text{NMAD}}$  above the median flux for both the image and the spectrum for that spaxel, as well as the presence of an adjacent pixel flagged by the pipeline, where  $\sigma_{\text{NMAD}}$  is defined as the normalized median absolute deviation.

We present false-color images of the IFU data cubes collapsed along the wavelength axis in Figure 1, along with the extracted 1D spectra. We create these images by taking the mean value for the flux of each pixel in the wavelength ranges of (6250Å, 7500Å), (4000Å, 5600Å) and (3735Å, 4000Å) for the red, green and blue channels, respectively. The integrated 1D spectra are extracted by coadding the flux from all the spaxels within an ellipse corresponding to the circularized half-light radius ( $R_e$ ). We additionally coadd spaxels in elliptical annuli with widths of  $\frac{1}{3}$  of the semi-major axis ( $R_{e,\text{maj}}$ ), equivalent to  $\sim 1$  pixel for each galaxy. This is done for 5 bins for each MQG, with the furthest annuli extending to  $\frac{5}{3}R_{e,\text{maj}}$ . Integrated 1D spectra for each MQG are shown in Appendix A.

These galaxies are among the most massive ( $11.23 \lesssim \log(M_*/M_\odot) \lesssim 11.50$ ) of the MAGAZ3NE survey, which targeted 32 galaxies. To highlight this, we present the size versus mass plot for the three MQGs in this study, along with those from similar studies in literature in Figure 2, colored by redshift. The galaxies in this study are both more massive and more compact than those at lower- $z$ . This informs us that the galaxies in our sample are not evolutionarily linked to those shown in lower- $z$  studies. This is discussed further in Section 5.1.4.

### 3. METHODS

#### 3.1. *Bagpipes SED Fitting*

We use the Bayesian Analysis of Galaxies for Physical Inference and Parameter ESTimation (BAGPIPES<sup>19</sup>; A. C. Carnall et al. 2018, 2019) to perform spectral fitting. BAGPIPES models complex galaxy properties and star formation histories within a Bayesian framework (A. C. Carnall et al. 2018, 2019). We use the default stellar library, the 2016 version of the G. Bruzual & S. Charlot (2003) stellar population models. We note that this stellar library assumes solar-scaled abundances.

We adopt a flexible non-parametric SFH with  $N=10$  time bins to capture potential early bursts using the Dense Basis (K. G. Iyer et al. 2019) implementation in BAGPIPES. This method reconstructs galaxy star formation histories using Gaussian Processes. This Gaussian Process SFH (GP-SFH) is parameterized as the stellar mass, star formation rate (SFR), and  $N$  lookback times ( $\{t_x\}$ ) corresponding to when the galaxy formed stellar mass fractions (i.e.,  $t_{10}$  corresponds to the lookback time when 10% of the total stellar mass is formed,  $t_{20}$  corresponds to the lookback time at which 20% was formed, etc). These lookback times have a Dirichlet prior (K. G. Iyer et al. 2019), and a corresponding  $\alpha$  concentration parameter. When  $\alpha < 1$ , lookback times are allowed to be granular, resulting in ‘bursty’ SFHs. When  $\alpha > 1$ , the lookback times are more evenly spaced out, which results in smoother SFHs (K. G. Iyer et al. 2019). Similar to M. L. Hamadouche et al. (2026b), we set  $\alpha = 30$  in the most recent time bin, and  $\alpha = 3$  in the remaining 9. This is to avoid the ‘first-bin burstiness’ that can affect the BAGPIPES implementation of Dense Basis (see I. McConachie et al. 2025a).

We assume a D. Calzetti et al. (2000) dust attenuation law, and an AGN component for XMM-VID3-2457 due to the presence of [O III] $\lambda\lambda 4959, 5007$  ( $EW_{\text{rest}} = 3.6$  Å) and [N II] $\lambda\lambda 6548, 6584$  ( $EW_{\text{rest}} = 3.5$  Å) emission lines. Instrumental dispersion is accounted for by incorporating the wavelength-dependent resolution curve for JWST/NIRSpec IFU G235M/F170LP into the fit. The priors are summarized in Appendix B.1. In short, we vary redshift, velocity dispersion, stellar mass, SFR, metallicity, dust attenuation, and the nebular ionization parameter,  $\log_{10}(U)$ . We use the same Gaussian Process (GP) noise model first presented in (H.-H. Leung et al. 2024). This model uses *celerite2* (D. Foreman-Mackey et al. 2017; D. Foreman-Mackey 2018) and its SHOTerm kernel for correlated and white noise. This GP noise model is treated as an additive term to the

<sup>19</sup> <https://github.com/ACCarnall/bagpipes>

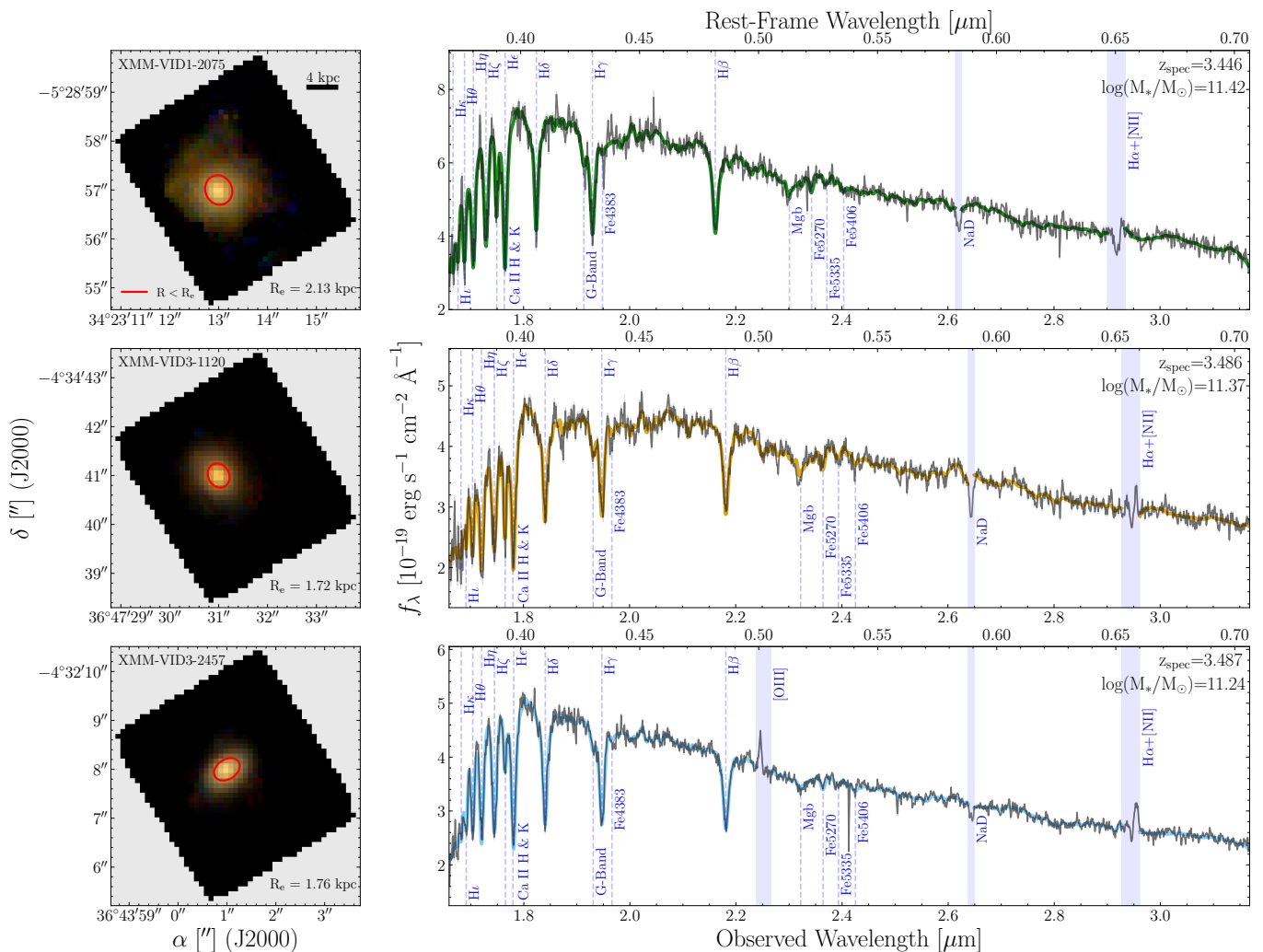


**Figure 1.** *Left:* False-color images of the MAGAZ3NE massive quiescent galaxies. We collapse the IFU data cubes along the wavelength axis and take the mean value for each pixel in the wavelength ranges of (6250Å, 7500Å), (4000Å, 5600Å) and (3735Å, 4000Å) for the R, G and B channels, respectively. We outline the effective radius ( $R_e$ ) of each galaxy in red and list the circularized  $R_e$  in kpc from B. Forrest et al. (2026) in the bottom right. All three galaxies are very compact, with  $R_e \lesssim 2$  kpc. Of particular note is XMM-VID1-2075, whose image shows low-surface brightness structure, indicative of a recent major merger. *Right:* Integrated ( $R < 1R_e$ ) 1D spectra with select spectral features highlighted. The associated uncertainty is shown in gray. Regions masked during SED fitting are shaded. The best-fit  $\alpha\text{IFe}$  models are plotted as well (XMM-VID1-2075, green; XMM-VID3-1120, gold; XMM-VID3-2457, blue). The galaxies all exhibit strong Balmer breaks and deep Balmer absorption lines, indicative of recently-quenched stellar populations.

spectrum to account for observational uncertainties and mismatched stellar spectral models.

To ensure that our results are robust to the choice of SFH prior (see K. A. Webb et al. 2022), we additionally adopt the continuity model (J. Leja et al. 2019) integrated into BAGPIPES. This model allows the user to set their own  $N$  time bins and their widths, and fits directly for the difference in SFR between adjoining bins. The continuity model does this by assuming a student- $t$  distribution on the quantity  $x = \log(\text{SFR}_n/\text{SFR}_{n+1})$ , where  $n$  refers to a given time bin (J. Leja et al. 2019). The GP-SFH model is better at capturing bursty or

episodic star formation histories (K. G. Iyer et al. 2019), while the continuity model prefers smoother histories unless required by the data. As both models encode different star formation history parameterizations, agreement between them would suggest that our results are data-driven rather than prior-dominated.

J. Leja et al. (2019) showed that when  $N \gtrsim 4$ , SFH results are insensitive to this choice. Similarly, K. G. Iyer et al. (2019) showed that  $N = 3$  is sufficient to recover SFHs, but the accuracy increases with  $N$ . With the high quality of spectra available to us, we are able to test the sensitivity of our SFH constraints to the adopted non-

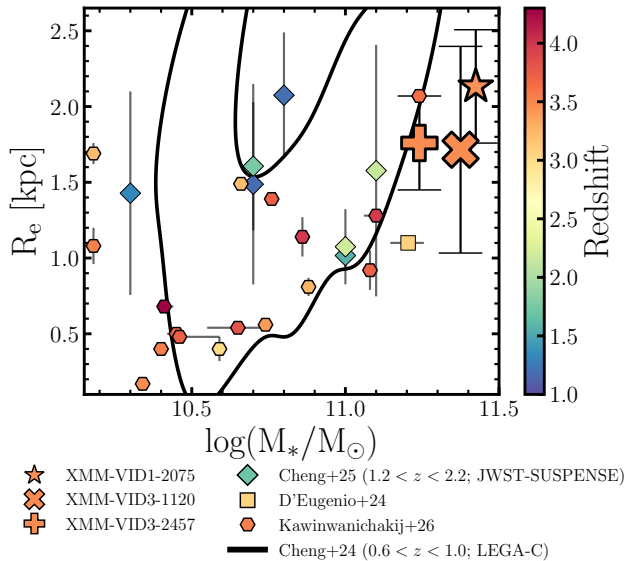


**Figure 2.** Size vs. mass comparison of massive quiescent galaxies both from this work and in literature, colored by redshift. Galaxies used in C. M. Cheng et al. (2025) from JWST-SUSPENSE (M. Slob et al. 2024) are shown as diamonds, and the galaxy studied in F. D’Eugenio et al. (2024) is shown as a square, with reported error bars. Galaxies from L. Kawinwanichakij et al. (2026) are shown as hexagons, using the inferred  $R_e$  from F277W JWST observations. Contours show the 1 and  $2\sigma$  contours for the LEGA-C (A. van der Wel et al. 2021) massive quiescent galaxy sample from C. M. Cheng et al. (2024), with masses taken from A. de Graaff et al. (2021).

parametric parameterization. For this reason, we use 10 time bins in our implementation of the continuity SFH model. The first 3 bins are spaced out linearly by 50 Myr, while the remaining bins are spaced out equally in log-space to the time of observation. We fix the redshift to the posterior median value from the GP-SFH fit for each MQG. We adopt a scale factor of  $\sigma = 0.7$  to balance between bursty and smooth SFHs. We also set the degrees of freedom  $\nu = 2$  as in J. Leja et al. (2019). Elsewhere, we fit for stellar population parameters in a similar manner as the GP-SFH fit (see Appendix B.1).

### 3.2. $\alpha\alpha$

The ultimate goal of SED fitting is to infer stellar population parameters and SFHs, but the age-dust-metallicity degeneracy limits any interpretation that is unable to break it. As most SED fitting codes use solar-scaled models, it is difficult to accurately constrain metallicities. Solar-scaled models do not capture variations in different elemental species, such as  $\alpha$ -elements. However, chemical abundance codes address this by allowing elemental abundances to vary, and therefore bet-

ter disentangle the metallicity from degeneracies with other elements.

We use  $\alpha\alpha$ <sup>20</sup> (A. Beverage 2024; A. G. Beverage et al. 2025) to derive ages,  $[\alpha/\text{Fe}]$  & metallicity.  $\alpha\alpha$  is a Python version of the full-spectrum fitting code Absorption Line Fitter (ALF; C. Conroy & P. G. van Dokkum 2012; C. Conroy et al. 2018), and incorporates the same single stellar population (SSP) models and elemental response functions presented in C. Conroy et al. (2018). The SSPs are built from both the empirical MILES (P. Sánchez-Blázquez et al. 2006) and extended IRTF (A. Villaume et al. 2017) stellar libraries, and utilize the MIST v1.2 (J. Choi et al. 2016) isochrones. Additionally, to obtain elemental abundances, C. Conroy et al. (2018) provided response functions for 19 elements.  $\alpha\alpha$  models the SFH as a single burst, effectively returning an SSP-equivalent age.

However, the C. Conroy et al. (2018) models are restricted to stellar populations that are older than 1 Gyr, and so are not appropriate for fitting the young quiescent galaxies observed at high redshift (i.e., A. Muzzin et al. 2014; S. Belli et al. 2019; C. M. Cheng et al. 2025; A. G. Beverage et al. 2025). Fortunately,  $\alpha\alpha$  has additionally adopted the sMILES (A. T. Knowles et al. 2021, 2023) SSPs, which incorporate models as young as 0.03 Gyr, making them ideal for studying these galaxies. Furthermore, sMILES grids span  $-1.5 < [Z/H] < +0.26$  ratios, allowing for analyses that span a large range in total metallicities. From this, we can infer  $[\text{Fe}/\text{H}]$  using Equation 2 from A. T. Knowles et al. (2023).

sMILES also spans  $-0.2 < [\alpha/\text{Fe}] < +0.6$  ratios, which is important, as the galaxies in this study are all recent PSB galaxies at high- $z$ . They have likely not had time for SNe Ia to enrich Fe throughout the galaxy, and therefore should be  $\alpha$ -enhanced (i.e., L. C. Kimmig et al. 2025). To do this, sMILES uses BaSTI solar-scaled isochrones (A. Pietrinferni et al. 2004) for the  $[\alpha/\text{Fe}] = -0.20, 0.0, \& +0.20$  SSPs, and the BaSTI  $\alpha$ -enhanced isochrones (A. Pietrinferni et al. 2006) for the  $[\alpha/\text{Fe}] = +0.40$  and  $+0.60$  SSPs (A. T. Knowles et al. 2023). sMILES varies the  $\alpha$  elements O, Ne, Mg, Si, S, Ca and Ti in lock-step (A. T. Knowles et al. 2021, 2023).

To understand the systemic differences between stellar population parameters recovered between the C. Conroy et al. (2018) grids and sMILES grids, we fit a mock galaxy spectrum with both libraries. We discuss this testing in detail in Appendix C. We find that there is a persistent systemic difference of  $\approx 0.1$  dex between the two grids for both  $[\text{Fe}/\text{H}]$  and  $[\alpha/\text{Fe}]$ . This is to

<sup>20</sup> <https://github.com/alizabeverage/alfalpha>

be expected, as different isochrones alone would naturally lead to different model spectra. However, quantifying this offset informs of the significance of this difference. Similar model-dependent offsets have been shown in M. Jafariyazani et al. (2025), with an average offset of  $\approx 0.1$  dex between  $[\alpha/\text{Fe}]$  inferred from the MILES (A. Vazdekis et al. 2015) and C. Conroy et al. (2018) models, and an average offset of  $\approx 0.3$  dex between inferred  $[\text{Fe}/\text{H}]$  values. This is more extreme than the difference we find between the sMILES and C. Conroy et al. (2018) grids, but highlights the need for future work investigating such systematic model uncertainties.

We use `alf $\alpha$`  with the sMILES grids, assuming a P. Kroupa (2001) IMF. We utilize `emcee` (D. Foreman-Mackey et al. 2013) for posterior sampling, and provide priors in Appendix B.1. We mask out the Na D $\lambda$ 5890, 5896 absorption feature, as well as the H $\alpha$ + [N II] complex for our fitting. We additionally mask out the [O III] $\lambda$  $\lambda$ 4959, 5007 doublet for XMM-VID3-2457. As discussed in A. G. Beverage et al. (2025), `alf $\alpha$`  estimates the continuum by fitting a Chebyshev polynomial to the data-to-model ratio, applied independently in wavelength ‘chunks’. Unless otherwise specified, the default mode is to add one extra degree to the polynomial for each 100 Å in the chunk, rounded up (i.e., `alf $\alpha$`  would use a 6th degree polynomial for a chunk of size 550 Å). A. G. Beverage et al. (2025) notes that results are robust to the choice of polynomial order. Nevertheless, to ensure consistency across radial bins and to avoid continuum subtraction systematics, we use identical wavelength chunks for all radial extractions within a given galaxy. Finally, we visually inspect the continuum fit after each run to verify the fit quality.

We note that rotational effects could impact our fitting results, particularly for XMM-VID3-2457, which is a fast rotator (B. Forrest et al. 2026). At larger radii, annular bins span greater rotational velocities, introducing additional spectral broadening that may bias measurements of stellar population parameters that are sensitive to line widths. This broadening is accounted for by the velocity dispersion fit, which assumes a Gaussian line-of-sight velocity distribution. Deviations from a true Gaussian profile are expected to be small and are therefore folded into the fit uncertainties and noise model.

## 4. RESULTS

### 4.1. Integrated Spectral Fits

We present the spectral fitting results for the extracted 1D spectra within  $1 R_e$  for each MQG. Table 1 lists the BAGPIPES results for both SFH models, while Table 2 summarizes the `alf $\alpha$`  results. XMM-VID1-2075 and XMM-VID3-1120 are both dust-poor, with

$A_V = 0.04_{-0.03}^{+0.04}$  and  $0.07_{-0.04}^{+0.04}$ , respectively, while XMM-VID3-2457 has an  $A_V = 0.34_{-0.04}^{+0.03}$ . These measurements are consistent with results from W. Chang et al. (2026), which studied the dust continuum of these three galaxies using ALMA observations. They found that XMM-VID1-2075 and XMM-VID3-1120 are extremely dust-poor, with  $M_{\text{dust}}/M_* \lesssim 10^{-4}$ . XMM-VID3-2457 is relatively dust-rich in the context of MQGs, with  $M_{\text{dust}}/M_* \sim 10^{-3}$ , approximately two dex below the main sequence (W. Chang et al. 2026).

Both `alf $\alpha$`  and BAGPIPES show that the MQGs are young ( $t_{\text{MW}} < 0.7$  Gyr) and extremely massive ( $M_* \gtrsim 10^{11} M_\odot$ ) for their epoch, similar to what has been shown for these MQGs in previous works using Keck/MOSFIRE spectroscopy (B. Forrest et al. 2020b, 2022, 2024). They also have large velocity dispersions ( $\sigma_* \gtrsim 330$  km/s), consistent within  $1\sigma$  of previous measurements from B. Forrest et al. (2022).

We also determine quenching times ( $t_q$ ) from the SFH. BAGPIPES defines  $t_q$  as when the following condition is satisfied in the galaxies history:

$$\text{nSFR}(t) = \frac{t_H \times \text{SFR}}{M_*} < 0.1 \quad (1)$$

where nSFR is the dimensionless normalized star-formation rate,  $t_H$  is the age of the Universe, and  $M_*$  the mass formed by the galaxy by time  $t_H$  (A. C. Carnall et al. 2018). All three galaxies are recently quenched, with inferred quenching times of  $\Delta t_q = t_{\text{obs}} - t_q = 0.24_{-0.03}^{+0.03}$  Gyr,  $0.15_{-0.06}^{+0.04}$  Gyr, and  $0.11_{-0.07}^{+0.02}$  Gyr before observation for XMM-VID3-1120, XMM-VID1-2075 and XMM-VID3-2457, respectively. The short separation between mass build-up and quenching ( $t_q - t_{50} \lesssim 500$  Myr) indicates that they experienced rapid assembly just prior to quenching. This is similar to what is shown in A. C. Carnall et al. (2024) for comparable galaxies at a similar epochs, supporting a picture where high- $z$  massive quiescent systems undergo intense, short-lived starbursts followed by rapid quenching. We discuss this in further detail in Sec. 4.1.2.

Given their extreme masses and compact nature ( $R_e \approx 2$  kpc), these MQGs have surface densities of  $\Sigma_* = (1.8 - 2.6) \times 10^{10} M_\odot \text{kpc}^{-2}$ , comparable with the core densities of local ellipticals ( $\Sigma_* \approx 10^{10} - 10^{11} M_\odot \text{kpc}^{-2}$ ; P. F. Hopkins et al. 2010; P. G. van Dokkum et al. 2010; M. Mosleh et al. 2017). These high surface densities support a two-phase growth scenario, wherein these early, compact systems form the high-density cores of today’s most massive ellipticals, with their subsequent structural growth occurring primarily through minor mergers (R. Bezanson et al. 2009; L. Oser et al. 2010; K. A. Suess et al. 2020).

## BAGPIPES

K. G. Iyer et al. (2019) SFH

Galaxy	$z_{\text{spec}}$	$\log(M_*/M_\odot)$	$\sigma_*$ (km s $^{-1}$ )	$\log(Z/Z_\odot)$	$A_V$	SFR $_{100}$ (M $_\odot$ yr $^{-1}$ )	$t_{\text{MW}}^a$ (Gyr)
XMM-VID1-2075	$3.4465^{+0.0002}_{-0.0002}$	$11.42^{+0.02}_{-0.01}$	$334^{+14}_{-15}$	$0.33^{+0.11}_{-0.10}$	$0.04^{+0.04}_{-0.03}$	$0.00^{+0.03}_{-0.00}$	$0.59^{+0.04}_{-0.04}$
XMM-VID3-1120	$3.4863^{+0.0003}_{-0.0003}$	$11.37^{+0.01}_{-0.01}$	$336^{+16}_{-13}$	$0.40^{+0.04}_{-0.03}$	$0.07^{+0.04}_{-0.04}$	$1.77^{+0.43}_{-0.41}$	$0.65^{+0.03}_{-0.02}$
XMM-VID3-2457	$3.4868^{+0.0002}_{-0.0002}$	$11.24^{+0.01}_{-0.01}$	$341^{+10}_{-12}$	$0.19^{+0.07}_{-0.07}$	$0.34^{+0.03}_{-0.04}$	$1.21^{+0.40}_{-0.34}$	$0.46^{+0.03}_{-0.03}$
J. Leja et al. (2019) SFH							
XMM-VID1-2075	Fixed	$11.42^{+0.01}_{-0.01}$	$328^{+14}_{-13}$	$0.19^{+0.07}_{-0.08}$	$0.04^{+0.05}_{-0.03}$	$0.05^{+0.74}_{-0.05}$	$0.55^{+0.04}_{-0.03}$
XMM-VID3-1120	Fixed	$11.36^{+0.01}_{-0.01}$	$334^{+11}_{-12}$	$0.35^{+0.02}_{-0.03}$	$0.09^{+0.03}_{-0.04}$	$1.30^{+0.91}_{-0.45}$	$0.60^{+0.03}_{-0.02}$
XMM-VID3-2457	Fixed	$11.22^{+0.01}_{-0.01}$	$339^{+12}_{-14}$	$0.19^{+0.05}_{-0.05}$	$0.43^{+0.03}_{-0.04}$	$5.52^{+4.41}_{-2.31}$	$0.34^{+0.02}_{-0.02}$

<sup>a</sup>mass-weighted age

**Table 1.** Posterior medians and  $1\sigma$  uncertainties from BAGPIPES, assuming a flexible, non-parametric Gaussian Process SFH model (K. G. Iyer et al. 2019) (top three rows) and a smooth, continuity SFH model (J. Leja et al. 2019) (bottom three rows). Continuity model fits assume the median posterior redshift from K. G. Iyer et al. (2019) SFH results. Fit results from both SFH models agree, with the exception of  $\log(Z/Z_\odot)$  and  $t_{\text{MW}}$ . This confirms that our results are robust to choice of SFH prior. Results for each galaxy are from our integrated ( $R < 1R_e$ ) spectral extraction. Star formation rates are reported as the 100 Myr-averaged rate (SFR $_{100}$ ). All three galaxies are very massive ( $\log(M_*/M_\odot) > 11.2$ ), have large velocity dispersions ( $\sigma_* \gtrsim 330$  km/s), are metal-rich ( $\log(Z/Z_\odot) \gtrsim 0.2$ ), and have little-to-no dust ( $A_V \lesssim 0.4$ ).

alf $\alpha$					
Galaxy	$t_{\text{SSP}}$ (Gyr)	[Fe/H]	[Z/H]	[ $\alpha$ /Fe]	$\sigma_*$ (km s $^{-1}$ )
XMM-VID1-2075	$0.63^{+0.06}_{-0.06}$	$-0.05^{+0.10}_{-0.12}$	$+0.04^{+0.11}_{-0.11}$	$+0.13^{+0.09}_{-0.08}$	$332^{+16}_{-15}$
XMM-VID3-1120	$0.69^{+0.09}_{-0.04}$	$+0.06^{+0.07}_{-0.08}$	$+0.11^{+0.09}_{-0.13}$	$+0.08^{+0.08}_{-0.20}$	$353^{+14}_{-13}$
XMM-VID3-2457	$0.53^{+0.03}_{-0.04}$	$+0.04^{+0.08}_{-0.09}$	$+0.03^{+0.09}_{-0.09}$	$-0.02^{+0.05}_{-0.05}$	$388^{+12}_{-12}$

**Table 2.** alf $\alpha$  fitting results, using  $\alpha$ -enhanced (sMILES) stellar population models. Ages are SSP-equivalent ( $t_{\text{SSP}}$ ). [Z/H] is the logarithmic abundance ratio of all metals relative to hydrogen, compared to the solar ratio. The MQGs are very young ( $t_{\text{SSP}} \lesssim 700$  Myr), and have metallicities that are consistent within  $1\sigma$  of solar abundances. XMM-VID1-2075 and XMM-VID3-1120 are both moderately  $\alpha$ -enhanced, while XMM-VID3-2457 is consistent with a solar [ $\alpha$ /Fe]. alf $\alpha$  also finds large velocity dispersions ( $\gtrsim 330$  km/s) for all three MQGs, consistent with their extreme stellar masses.

4.1.1. *Metallicities*

The integrated spectra of XMM-VID1-2075 and XMM-VID3-1120 are moderately  $\alpha$ -enhanced ( $[\alpha/\text{Fe}] = +0.13^{+0.09}_{-0.08}$  and  $+0.08^{+0.08}_{-0.20}$ , respectively). This is consistent with literature showing that post-starburst galaxies are  $\alpha$ -enhanced due to recent and rapid star-formation (i.e., M. Kriek et al. 2016; A. G. Beverage et al. 2024, 2025; L. C. Kimmig et al. 2025; N. M. Gountanis et al. 2025; I. McConachie et al. 2025a; M. L. Hamadouche et al. 2026b). However, these [ $\alpha$ /Fe] values are relatively low compared to other MQGs observed in literature, which generally exceed [ $\alpha$ /Fe]  $\gtrsim +0.3$  (i.e., M. Kriek et al. 2016; A. G. Beverage et al. 2024, 2025; N. M. Gountanis et al. 2025; I. McConachie et al. 2025a; M. L. Hamadouche et al. 2026b). Furthermore, XMM-VID3-2457 is consistent within  $1\sigma$  of a solar abundance pattern ( $[\alpha/\text{Fe}] = -0.02^{+0.05}_{-0.05}$ ). While this is somewhat surprising, M. L. Hamadouche et al. (2026b) observe a spread in [ $\alpha$ /Fe] abundance ratios ( $[\alpha/\text{Fe}] = +0.22^{+0.22}_{-0.17}$ ) for MQGs at this epoch. This may be due to early AGN outflows. As the ISM would not yet have been en-

riched in Fe-peak elements by SNe Ia, these outflows would preferentially eject  $\alpha$ -elements, which would have already been present. This would naturally lower the observed [ $\alpha$ /Fe].

Additionally, M. L. Hamadouche et al. (2026b) notes that while SNe Ia have long enrichment timescales, their delay-time distribution (DTD) after a star-formation event follows a power law that is  $\text{DTD}(\tau) \propto \tau^{-1}$  (G. De Lucia et al. 2014). This allows for the onset of chemical enrichment from SNe Ia to occur as early as  $\sim 40$  Myr after such a star formation event, the minimum time for white dwarfs to form. Fe-peak elements would then be enriched earlier than expected. The [ $\alpha$ /Fe] abundance ratio in the galaxy would then be correspondingly reduced once the Fe-enriched gas is incorporated into new stars. For more discussion on this, see M. L. Hamadouche et al. (2026b). Alternatively, prior SNe Ia enrichment before the recent burst of star-formation could have enriched the stellar population with Fe-peak elements. This is consistent with the supersolar metallicities reported from BAGPIPES.

Disconcertingly, the metallicities inferred from BAGPIPES and `alf $\alpha$`  are offset by  $\approx 0.2-0.4$  dex (Tables 1 & 2). Recent literature has found similar offsets between codes using solar-scaled libraries and those that allow for variable elemental abundances. [A. G. Beverage et al. \(2025\)](#) compared the metallicities from `Prospector` ([J. Leja et al. 2019](#); [B. D. Johnson et al. 2021](#)), which uses solar-scaled stellar libraries, to metallicities from `alf $\alpha$` , using the [C. Conroy et al. \(2018\)](#) grid to vary individual elemental abundances. They found a large scatter, with offsets up to  $\approx 0.7$  dex. Similarly, [I. McConachie et al. \(2025a\)](#) found a  $\approx 0.15$  dex offset between `Prospector` and `alf $\alpha$`  metallicities. [H.-H. Leung et al. \(2026a\)](#) confirmed this is also the case between BAGPIPES and `alf $\alpha$`  (using the `sMILES` grids), finding offsets as large as  $\approx 0.7$  dex. While the disagreement between the metallicities found in this work are less severe than what is presented in other literature, this emerging trend is concerning, and future work is needed to reconcile it.

A secondary effect that can contribute to this offset is the difference in zero-point solar abundances assumed between BAGPIPES and `alf $\alpha$` , based on the choice of stellar library. BAGPIPES utilizes the 2016 version of the [G. Bruzual & S. Charlot \(2003\)](#) stellar population models, which adopts the `MILES` ([J. Falc3n-Barroso et al. 2011](#); [A. Vazdekis et al. 2015](#)) library of empirical spectra. `MILES` assumes a solar metallicity of  $Z_{\odot} = 0.0198$  from [N. Grevesse & A. Noels \(1993\)](#). `sMILES` uses the `BaSTI` isochrones, which in turn also assumes the [N. Grevesse & A. Noels \(1993\)](#) value for  $Z_{\odot}$ . However, `sMILES` adopts the [M. Asplund et al. \(2005\)](#) solar abundances for their theoretical stellar spectra, which has  $Z_{\odot} = 0.0122$ . Equation 2 in [A. T. Knowles et al. \(2023\)](#) accounts for this by converting their SSP values to the [N. Grevesse & A. Noels \(1993\)](#) abundances so that they are using the right isochrone. Importantly, [A. T. Knowles et al. \(2023\)](#) notes that this conversion is not fully consistent, resulting in different  $\alpha$ -element abundances. However, they note that this is a secondary effect to the choice in stellar spectra to use ([A. Vazdekis et al. 2015](#)).

#### 4.1.2. Ages & Mass Build-up

We present the SFH and Mass Assembly History for each galaxy in Figure 3. All three MQGs experienced a recent, intense starburst, with star-formation rates exceeding  $500 M_{\odot} \text{ yr}^{-1}$  within the 500 Myr prior to observation, corresponding to  $4 \lesssim z \lesssim 5$ . All three MQGs also assembled very early. XMM-VID3-2457 assembled  $\gtrsim 10\%$  of its total formed stellar mass ( $M_{*} \approx 10^{10} M_{\odot}$ ) by  $z \sim 6$ , while XMM-VID1-2075 and XMM-VID3-1120 both assembled  $\gtrsim 20\%$  of their total formed stellar mass ( $M_{*} \approx 10^{10.8} M_{\odot}$ ) during this same time. The

latter two nearly reach the ultra-massive galaxy regime ( $M_{*} \gtrsim 10^{11} M_{\odot}$ ) within the first  $\sim 1$  Gyr.

While the masses reported by BAGPIPES are extreme, they are consistent with the most massive galaxy expected in a survey the size of XMM-VIDEO ( $\sim 4.65 \text{ deg}^2$ ), as quantified by `evstats` ([C. C. Lovell et al. 2023](#)). `evstats` computes the probability density function of the most massive galaxy expected in the XMM-VIDEO survey volume ( $4.65 \text{ deg}^2$ ), assuming a baryon fraction  $f_b = 0.16$  and a  $\Lambda$ CDM cosmology ([C. C. Lovell et al. 2023](#)).

The GP-SFHs agree with the continuity fits at recent times. At early times ( $z \gtrsim 5$ ) however, the continuity model does not capture the predicted early mass growth from the GP-SFHs. We note that the amount of early mass growth is highly sensitive to the choice of scale factor in the continuity prior. Changing this to  $\sigma = 0.3$  results in excess mass in the early bins relative to what is physically allowed in  $\Lambda$ CDM. Alternatively,  $\sigma = 1.0$  results in most of the mass forming in 1-3 bins, consistent with the peaks observed in the GP-SFHs. We note that the fitting results from the continuity models are consistent within  $1-2\sigma$  with the GP-SFH results. Therefore, our main results are robust to the choice of SFH prior.

The choice of IMF can also impact inferred stellar masses. [C. M. Cheng et al. \(2026\)](#) showed that early, extremely massive galaxies could prefer a bottom-heavy IMF such as the [E. E. Salpeter \(1955\)](#) IMF. In contrast, BAGPIPES utilizes a [P. Kroupa & C. M. Boily \(2002\)](#) IMF, which would infer masses about 3-4 times less massive than the [E. E. Salpeter \(1955\)](#) IMF ([C. M. Cheng et al. 2026](#)). Our mass measurements are therefore conservative. Moreover, they are realistic for our sample, as [B. Forrest et al. \(2022\)](#) found that the dynamical masses for these MQGs prefers a ‘bottom-light’ IMF like [G. Chabrier \(2003\)](#).

## 4.2. Resolved Spectral Fits

### 4.2.1. Age, Metallicity, and $[\alpha/\text{Fe}]$ Gradients

We present radial gradients of age,  $[\text{Fe}/\text{H}]$ , and  $[\alpha/\text{Fe}]$  for each galaxy in Figure 4, and all together in Figure 5. We compare our results to those from JWST/NIRSpec slit spectra of the same sources from the *DeepDive* survey ([M. L. Hamadouche et al. 2026b](#)), which observed two of our three targets.

The gray shaded region represents the expected full width half max (FWHM) of the point spread function (PSF) at the red end of the spectrum, measured using `StPSF`. At the blue end, the PSF FWHM corresponds to  $\approx \frac{1}{2}$  pixel, or  $\approx 370$  pc at the redshift of the MQGs. At the red end of the spectrum, it corresponds to  $\approx 1$  pixel,

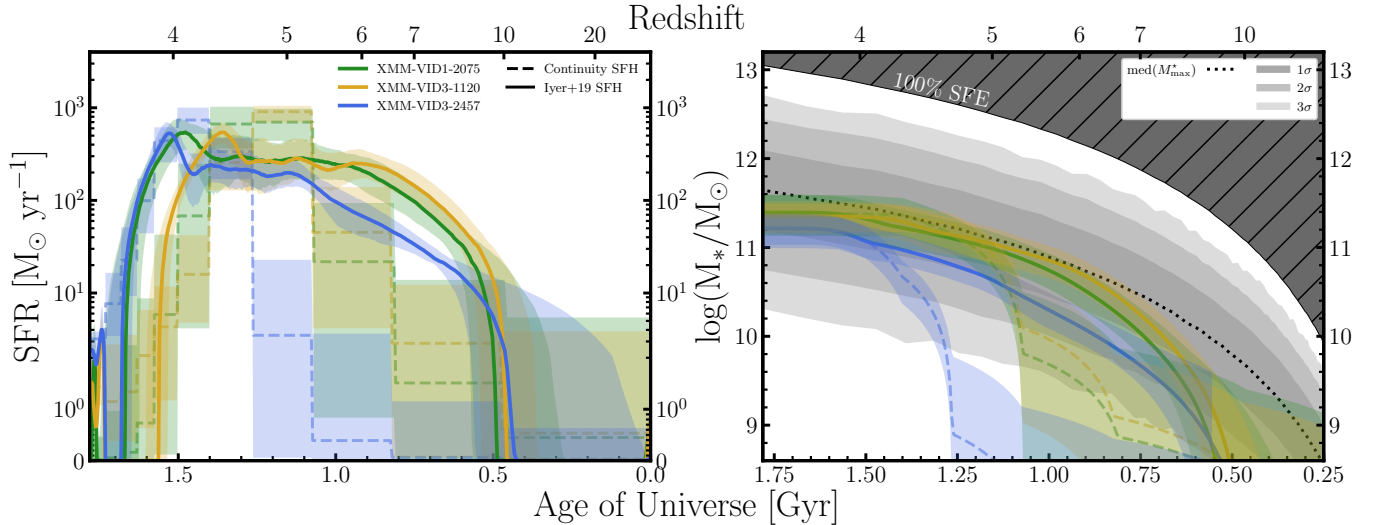


**Figure 3.** *Left:* BAGPIPES star-formation histories. Solid lines show the non-parametric Gaussian Process SFH (K. G. Iyer et al. 2019), and dashed lines show SFHs adopting the continuity model (J. Leja et al. 2019). *Right:* Mass assembly histories based on the inferred SFHs. We compare these with the probability density function of the most massive galaxy expected in the XMM-VIDEO survey volume (assuming an area of  $4.65 \text{ deg}^2$ ), computed using *evstats* (C. C. Lovell et al. 2023). The hatched region corresponds to where *evstats* requires 100% SFE at a  $> 3\sigma$  confidence level. All three galaxies formed early, reaching masses of  $\gtrsim 10^{10} M_\odot$  in the first  $\sim 800$  Myr of cosmic time ( $z \sim 6.8$ ). XMM-VID1-2075 and XMM-VID3-1120 both are approaching  $M_* \sim 10^{11} M_\odot$  by  $z \sim 6$ .

or  $\approx 730$  pc. We note that this change in PSF would flatten our derived stellar population gradients. Therefore, while a correction would result in steeper gradients, the directionality of the gradients would not change. Hence, our main results are robust against PSF effects.

We note that our integrated IFU measurements are consistent with those derived from MSA slit spectroscopy, although the IFU yields smaller uncertainties. However, in XMM-VID3-2457, the MSA-based results for  $[\text{Fe}/\text{H}]$  and  $[\alpha/\text{Fe}]$  better resemble IFU-based results from the core, rather than from the integrated measurements. The most likely cause of this is that the central portion of the galaxy dominates the light of the slit spectra. The slit width of the MSA is  $0.2''$ , while XMM-VID3-2457 has an effective radius  $R_e = 0.28''$ . Therefore, the integrated IFU results present a more complete look at the entire stellar population of these galaxies.

Our full spectrum fitting with *alf $\alpha$*  reveals that the cores ( $R \lesssim 0.5$  kpc) of each galaxy are young ( $t_{\text{SSP}} \lesssim 700$  Myr) and  $\alpha$ -enhanced ( $[\alpha/\text{Fe}] \gtrsim +0.2$ ), with XMM-VID1-2075 and XMM-VID3-1120 exhibiting solar metallicities ( $[\text{Fe}/\text{H}] = -0.03_{-0.06}^{+0.06}$  and  $[\text{Fe}/\text{H}] = +0.05_{-0.08}^{+0.07}$ , respectively). This implies that they formed via a similar process. The young ages and elevated  $[\alpha/\text{Fe}]$  indicate rapid, recent star-formation, suggesting a past starburst (e.g., L. C. Kimmig et al. 2025). Post-starburst regions show similar SFHs and analogous chemical enrichment properties, regardless of spa-

tial location within a galaxy (H.-H. Leung et al. 2025), suggesting that while the direct causes of the starburst might vary, they dominate local processes in the galaxy and result in comparable stellar populations. An extreme central starburst is therefore a likely explanation for these observations.

Beyond the cores, both XMM-VID1-2075 and XMM-VID3-1120 have positive age gradients and negative  $[\alpha/\text{Fe}]$  gradients. XMM-VID1-2075 also has a negative  $[\text{Fe}/\text{H}]$  gradient, while XMM-VID3-1120 has a roughly flat  $[\text{Fe}/\text{H}]$  gradient. XMM-VID3-2457, on the other hand, displays a flat age gradient. Outside of the central bin, it has negative  $[\text{Fe}/\text{H}]$  and positive  $[\alpha/\text{Fe}]$  gradients. It would appear that XMM-VID1-2075 and XMM-VID3-1120 have likely experienced an intense central starburst followed by strong feedback, causing rapid quenching. XMM-VID3-2457 seems to have quenched uniformly, plausibly by an AGN given the presence of  $[\text{O III}]\lambda\lambda 4959, 5007$  and  $[\text{N II}]\lambda\lambda 6548, 6584$  emission. Further discussion on the implications of these gradients can be found in Section 5.1.

We again note that rotational effects are a concern at larger radii, particularly for XMM-VID3-2457, which is a fast rotator (B. Forrest et al. 2026). To account for potential line broadening, we include velocity dispersion as a free parameter in our *alf $\alpha$*  fits. Although we assume a Gaussian shape, any offsets resulting from this functional form and the intrinsic line shape are small and fully accounted for in the noise modeling. Future

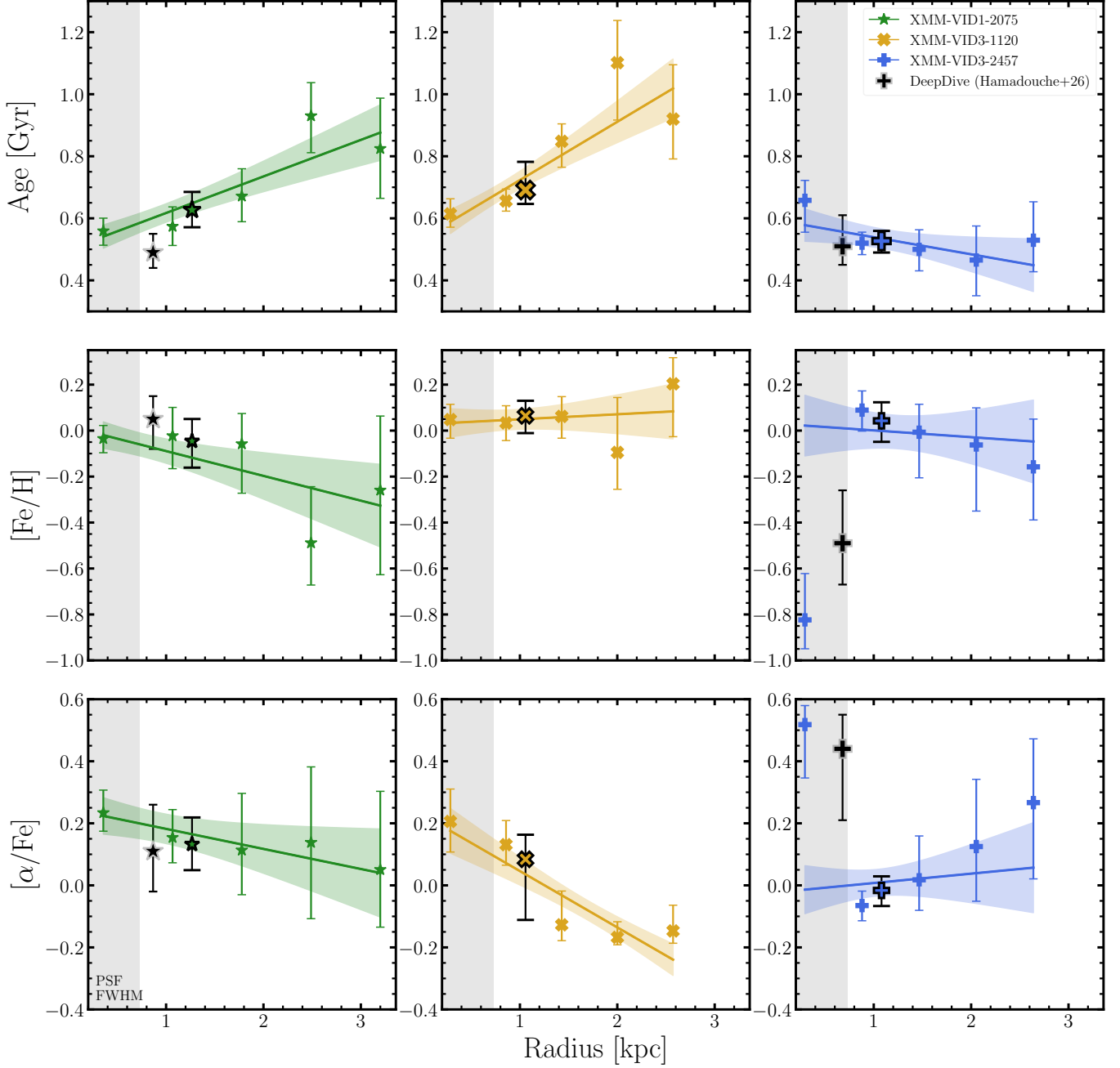


**Figure 4.** Age (*Top*), [Fe/H] (*Middle*), and [alpha/Fe] (*Bottom*) gradients for all three galaxies in this study. We outline measurements within  $R < 1R_e$  and plot them at  $\frac{1}{2}R_e$ , slightly shifted for visual purposes. The remaining points are measured in elliptical annuli centered around the galaxy, in bins with a semi-major axis width of 1 pixel. We illustrate gradients using a least-squares fit to the radial measurements. Additionally, we plot results from M. L. Hamadouche et al. (2026b), which observed two of our galaxies using NIRSpc MSA slit spectroscopy, as black points with a gray outline. The FWHM of the PSF at the red end of the spectrum ( $\sim 1$  pixel, or  $\text{FWHM}_{\text{PSF}} \approx 730\text{pc}$ ) is shown in gray.

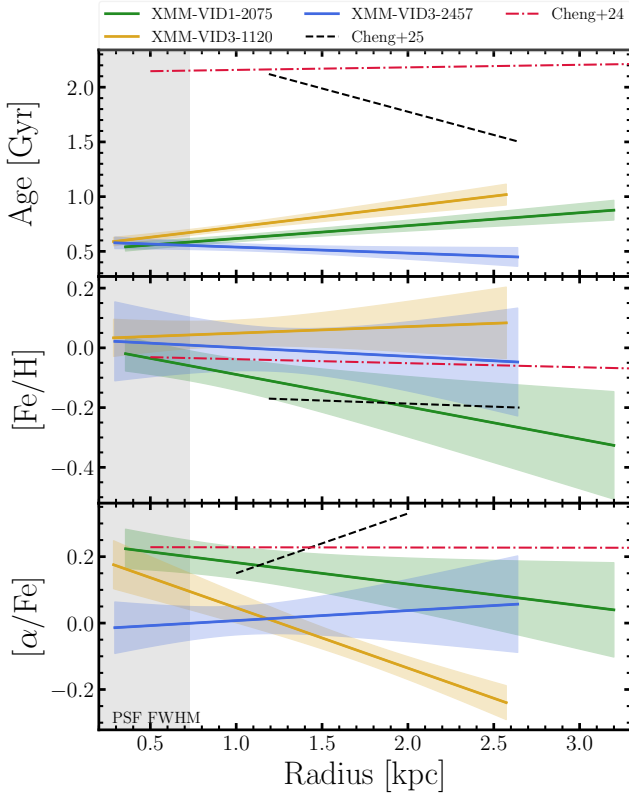


**Figure 5.** Same as Fig. 4, but with all galaxies plotted together for visual comparison. Data points are not shown for clarity, but we instead show the trend lines and associated uncertainties. We additionally show the median gradients from C. M. Cheng et al. (2025) for massive quiescent galaxies at  $1.2 < z < 2.2$  in JWST-SUSPENSE as a black dashed line for comparison. We also show the median gradients from the ‘young quiescent’ LEGA-C galaxies at  $0.6 < z < 1$  in C. M. Cheng et al. (2024) as a red dash-dotted line.

work will more thoroughly test this using velocity dispersion profiles. However, we note that the outermost bins are consistent with their respective trends, which is encouraging.

These gradients highlight the importance of IFU spectroscopy in studying the evolution of massive quiescent galaxies. The UVJ color evolution of these MQGs are roughly flat, with mean slopes of  $\langle \frac{d(\text{UV})_{\text{rest}}}{d \text{kpc}} \rangle = -0.02$  and  $\langle \frac{d(\text{VJ})_{\text{rest}}}{d \text{kpc}} \rangle = 0.04$ . As noted in C. M. Cheng et al. (2024), broad-band colors and low-resolution spectra would be unable to break the age-dust-metallicity degeneracy for such galaxies. However, with the high resolution spectra available from JWST/NIRSpec IFU, we can do so using absorption line diagnostics, allowing us to measure physically meaningful gradients.

#### 4.2.2. Resolved Star Formation Histories

We present the SFHs for each elliptical annular bin in Figure 6. The left panels show the SFHs, modeled using BAGPIPES, as described in Section 3.1. The right panels show the mass assembly history, calculated from the SFH. Both are in units of surface density. Like the integrated SFHs, the continuity and GP-SFHs are in good agreement near the time of observation. Above  $z \gtrsim 5$ , however, the continuity model does not predict the early mass growth the GP-SFH models do, similar to the disagreement seen in the integrated SFHs (Section 4.1.2). The radial SFHs for all three MQGs are consistent with an extreme central starburst ( $\Sigma_{\text{SFR}} \gtrsim 50 M_{\odot} \text{ yr}^{-1} \text{ kpc}^{-2}$ ) occurring between  $4 < z < 5$ , and substantial early mass growth above  $z \sim 6$ , similar to our integrated results. They also illustrate a more complicated picture of past quenching of the MQGs than previous observations (B. Forrest et al. 2020b).

All radial bins of XMM-VID3-2457 quench at the same time within uncertainties ( $t_{q, \text{core}} - t_{q, \text{outskirts}} = 60^{+44}_{-44}$  Myr), consistent with the pattern seen in the age gradients. XMM-VID3-1120 quenches in an inside-out pattern, where the central bins quench earlier than the outskirts ( $t_{q, \text{core}} - t_{q, \text{outskirts}} = 128^{+55}_{-41}$  Myr). Similar to XMM-VID3-2457, XMM-VID1-2075 quenches its annular bins at the same time within uncertainties ( $t_{q, \text{core}} - t_{q, \text{outskirts}} = 25^{+66}_{-83}$  Myr). This is puzzling, as this is counter to what is expected from the positive age gradient seen in XMM-VID1-2075 from  $\alpha$  fitting.

This difference is likely due to how the different stellar codes treat  $\alpha$ -elements. For example, the inner-most bin of XMM-VID3-2457 is the most  $\alpha$ -enhanced spectrum in our sample with  $[\alpha/\text{Fe}] = +0.52^{+0.06}_{-0.17}$ , which would indicate a formation time  $t_{\text{form}} = 12.4^{+117.1}_{-2.9}$  Myr using the relationship  $[\alpha/\text{Fe}] = \frac{1}{5} - \frac{1}{6} \log_{10}(\Delta t_{\text{form}}/\text{Gyr})$  (D. Thomas et al. 2005). In comparison, BAGPIPES SFH modeling shows that the formation timescale,  $\tau_{\text{SF}} = t_{80} - t_{20} = 423 \pm 68$  Myr. This is expected, as BAGPIPES uses solar-scaled stellar libraries, which do not consider how  $\alpha$ -enhancement can shorten formation timescales. Future work using  $\alpha$ -MC (M. Park et al. 2025) or incorporating sMILES into BAGPIPES as done in H.-H. Leung et al. (2026a) will be important to better constrain these timescales. Furthermore, as noted in H.-H. Leung et al. (2026b), making a distinction between ‘inside-out’, ‘outside-in’, and ‘uniform’ quenching is perhaps overly simplistic when compared to complex, spatially resolved SFHs. We discuss this further in Section 5.1.3.

Redshift

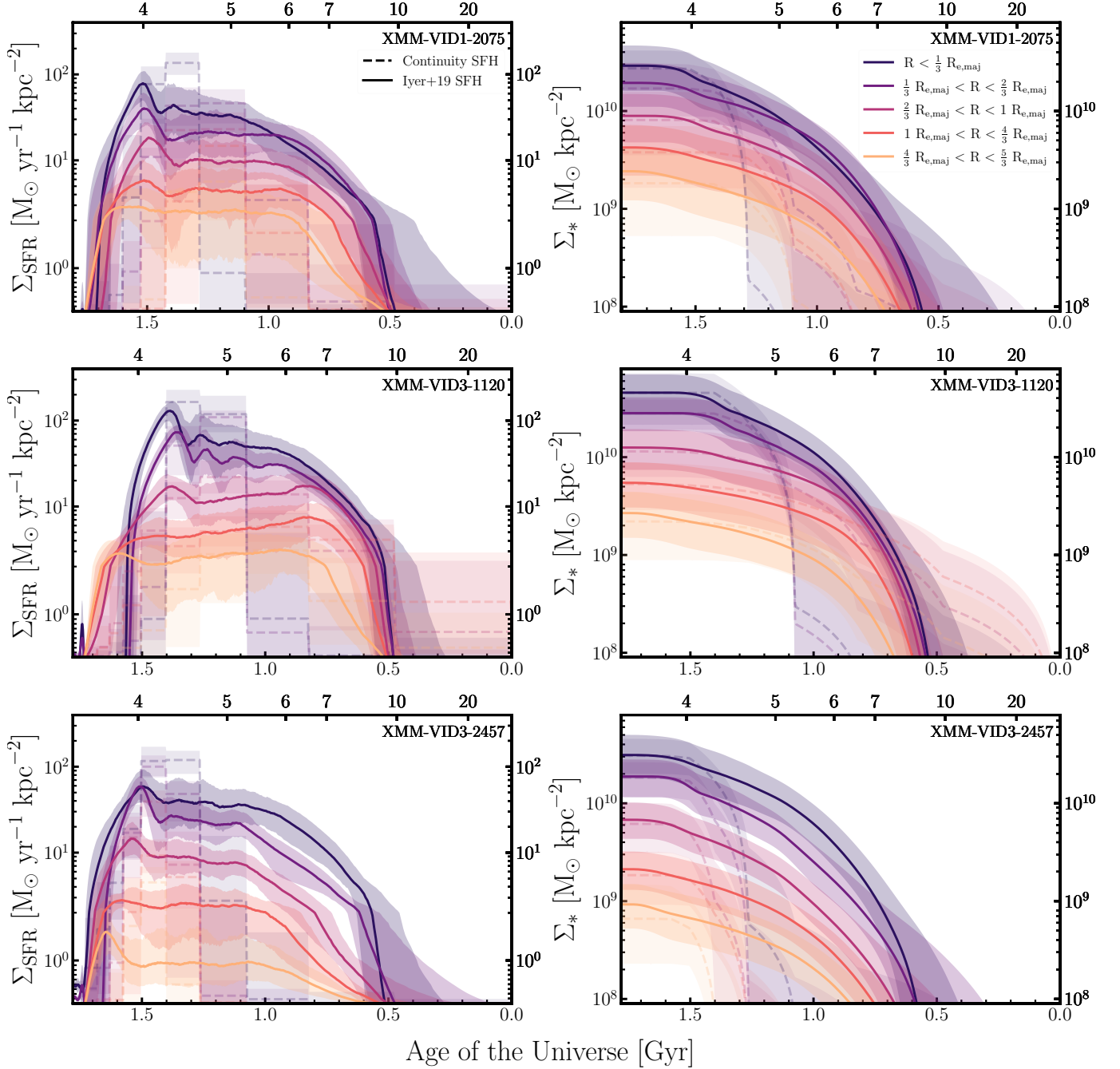


**Figure 6.** *Left:* Radial SFHs of each massive quiescent galaxy, modelled by BAGPIPES assuming a Gaussian Process SFH (K. G. Iyer et al. 2019) (solid lines) and continuity model (J. Leja et al. 2019) (dashed lines). *Right:* Mass assembly history as a function of cosmic time. Both are shown in units of surface density. Shaded regions correspond to  $1\sigma$  confidence intervals.

## 5. DISCUSSION

### 5.1. Formation Processes for MQGs at Early Times

#### 5.1.1. Central Starburst

In this paper, we have presented a spatially-resolved study of massive quiescent galaxies at  $z > 3$ . Our three targets are dominated by post-starbursts with remark-

ably similar stellar population properties. This homogeneity implies a potential common evolutionary pathway that formed the core of all three MQGs (H.-H. Leung et al. 2025). The young ( $t_{\text{SSP}} \lesssim 700$  Myr) ages and high  $[\alpha/\text{Fe}]$  ( $\gtrsim +0.2$ ) in these regions are consistent with a short but intense central starburst. Such a starburst would allow for significant SNe II enrichment

but little SNe Ia enrichment, elevating  $[\alpha/\text{Fe}]$ . This is reinforced by the radial SFHs (Fig. 6), which show that the cores all had extreme ( $\Sigma_{\text{SFR}} > 50 \text{ M}_{\odot} \text{ yr}^{-1} \text{ kpc}^{-2}$ ) star-formation rate densities at  $4 < z < 5$ .

The extreme star-formation rates inferred by the SFHs suggest an evolutionary link to sub-millimeter galaxies (SMGs) at  $4 \lesssim z \lesssim 6$  as the progenitors of MQGs at  $3 < z < 4$  (e.g., S. Toft et al. 2014; D. Marchesini et al. 2014; A. Wilkinson et al. 2017; C. Gómez-Guijarro et al. 2018; B. Forrest et al. 2020a; F. Valentino et al. 2020; A. C. Carnall et al. 2023a; K. Glazebrook et al. 2024; M. Skarbinski et al. 2026; P. Araya-Araya et al. 2026; J. A. Zavala et al. 2026). The inferred extreme star-formation rates and stellar masses of the MQGs between  $4 \lesssim z \lesssim 6$  agree within  $\sim 1\sigma$  of those reported for a sample of SMGs in COSMOS at this epoch ( $\text{SFR} \gtrsim 500 \text{ M}_{\odot} \text{ yr}^{-1}$ ,  $M_{*} \approx 10^{11} \text{ M}_{\odot}$ ; V. Smolčić et al. 2015), hinting further that SMGs may be their progenitors.

Recent theoretical work corroborates this picture. P. Araya-Araya et al. (2026) uses a recalibrated version of the L-Galaxies Semi-Analytical Model (P. Araya-Araya et al. 2025) that reproduces the observed number densities of both massive quiescent galaxies and SMGs. In their model, MQGs in the ultra-massive regime ( $M_{*} > 10^{11} \text{ M}_{\odot}$ ) were all sub-mm bright ( $S_{870} \gtrsim 1 \text{ mJy}$ ) at some point in their past. During the sub-mm bright phase, the MQGs experienced major mergers and black hole growth. As the gas reservoir empties from the starburst induced by the merger, AGN feedback stops further gas cooling (P. Araya-Araya et al. 2026). They find that  $z = 3$  and  $z = 4$  MQGs quench 0.6 Gyr and 0.4 Gyr after the peak sub-mm phase occurs. This is shorter than typical dust destruction timescales ( $\sim 100$  Myr; e.g., A. P. Jones & J. A. Nuth 2011), which implies that their descendants would be dust-poor when observed. This is the case for our sample, as they are dust-poor ( $A_V \lesssim 0.4$ ). ALMA Band 7 observations confirm this, as two are undetected, and XMM-VID3-2457 has only a faint  $870 \mu\text{m}$  dust continuum detection (W. Chang et al. 2026).

### 5.1.2. Difference in Gradients

We can see from Figure 4 that the MQGs exhibit different radial trends. To compare these radial trends, we construct nested models to quantify their independence.

We first build model M0, where each measurement parameter (age,  $[\text{Fe}/\text{H}]$ ,  $[\alpha/\text{Fe}]$ ) is fit with a single slope and intercept as a function of radius, fit using measurements from all three galaxies. We then build model M1, where each parameter for each MQG is assigned a slope that is shared among all three galaxies, but a unique intercept for each. We finally build model M2, where the

data for each galaxy are fit with an independent slope and intercept.

M2 would be preferred in a scenario where the MQGs have statistically different radial trends, both in intercept and slope for a given parameter. This would be expected in a scenario where the MQGs experienced significantly divergent evolutionary pathways. M0, alternatively, would be preferred if the MQGs exhibited similar gradients across all samples, implying they experienced near identical evolutionary effects throughout their volumes. M1 is preferred when the MQGs share a statistically similar slope but differ in normalization, implying the MQGs would have experienced similar processes with varying strengths or timescales.

We compare each model for each parameter using a  $\Delta\text{BIC}$  test (G. Schwarz 1978), where the Bayesian Information Criterion (BIC) is defined as:

$$\text{BIC} = k \ln(n) - 2L \quad (2)$$

where  $k$  is the number of parameters in a given model,  $n$  is the sample size, and  $L$  is the log-likelihood evaluated for the model. This provides a statistical test of how well the model fits the data, while penalizing overfitting. When comparing two models, the model with the lower BIC is preferred.  $0 < |\Delta\text{BIC}| \leq 2$  is considered weak evidence in favor of the model with a lower BIC,  $2 < |\Delta\text{BIC}| \leq 6$  is considered moderate evidence,  $6 < |\Delta\text{BIC}| \leq 10$  is considered strong evidence, and  $10 < |\Delta\text{BIC}|$  is considered very strong evidence (R. E. Kass & A. E. Raftery 1995).

We use `statsmodels` (S. Skipper & P. Josef 2010) to evaluate the log-likelihood for each model. For each parameter, M2 is found to have the lowest BIC, and M1 usually the second lowest. The only exception is for  $[\text{Fe}/\text{H}]$ , where M0 has a  $\text{BIC} = -8.8$  and M1 has  $\text{BIC} = -8.4$ . M2 is preferred strongly for age ( $\Delta\text{BIC} = 9.2$ ) and moderately for  $[\text{Fe}/\text{H}]$  ( $\Delta\text{BIC} = 2.5$ ) and  $[\alpha/\text{Fe}]$  ( $\Delta\text{BIC} = 5.8$ ) when compared to M1. When we exclude XMM-VID3-2457, we find that M1 is weakly preferred for both age ( $\Delta\text{BIC} = 1.8$ ) and  $[\text{Fe}/\text{H}]$  ( $\Delta\text{BIC} = 0.1$ ), and M2 is strongly preferred for  $[\alpha/\text{Fe}]$  ( $\Delta\text{BIC} = 10.7$ ). We therefore conclude that there is moderate to strong statistical evidence that XMM-VID3-2457 has statistically distinct radial trends than XMM-VID1-2075 and XMM-VID3-1120, both of which appear to have similar age and  $[\text{Fe}/\text{H}]$  trends. This would suggest that XMM-VID3-2457 has a distinct quenching pathway, while XMM-VID1-2075 and XMM-VID3-1120 seem to have undergone similar processes.

### 5.1.3. *Inside-out vs. Uniform Quenching*

We can quantitatively say from Section 5.1.2 that XMM-VID1-2075 and XMM-VID3-1120 exhibit statistically similar radial trends. XMM-VID1-2075 has a positive age gradient, a negative [Fe/H] gradient, and a mildly negative [ $\alpha$ /Fe] gradient. XMM-VID3-1120 exhibits a positive age gradient and a flat [Fe/H] gradient. It also has a very negative [ $\alpha$ /Fe] gradient, such that the outer radial bins push against the lower limit of the sMILES grids ( $[\alpha/\text{Fe}] = -0.2$ ). The flat [Fe/H] gradient suggests relatively uniform Fe enrichment across the galaxy, consistent with widespread SNe Ia enrichment prior to the central starburst which enriched the core with  $\alpha$ -elements.

Both galaxies have cores that are young and  $\alpha$ -enhanced. This is consistent with a scenario where, after a major merger, gas is compacted to the center of the galaxy, igniting a central starburst. Strong AGN feedback then suppresses the depleted gas reservoir from forming stars in the central regions (M. Park et al. 2023; W. McClymont et al. 2025; L. C. Kimmig et al. 2025; P. Araya-Araya et al. 2026; Y. Ni et al. 2025). This feedback propagates outwards, quenching the galaxy on short timescales ( $\sim 100 - 200$  Myr; F. D’Eugenio et al. 2020; M. Park et al. 2023; L. C. Kimmig et al. 2025; W. McClymont et al. 2025; Y. Ni et al. 2025). This is unlike inside-out quenching, which occurs on much longer timescales ( $\gtrsim 1$  Gyr; e.g., D. Walters et al. 2022; C. Lawlor-Forsyth et al. 2026). Rapid, merger driven quenching results in positive age gradients, as the centers have younger light-weighted ages from the starburst (P.-F. Wu et al. 2020; D. Pathak et al. 2021; Y. Ni et al. 2025), as seen in both XMM-VID1-2075 and XMM-VID3-1120.

XMM-VID1-2075 shows evidence of such a major merger capable of triggering an extreme starburst, with extended low-surface brightness morphological asymmetries and a low ( $\lambda_{R_e} \approx 0.1$ ) spin parameter (B. Forrest et al. 2026). It falls in the slow-rotator region of the spin parameter-ellipticity plane, very likely due to past major mergers (B. Forrest et al. 2026). Although XMM-VID3-1120 is not a slow rotator, it has a low spin parameter ( $\lambda_{R_e} \approx 0.3$ ) compared to XMM-VID3-2457, which is a fast rotator. Therefore, based on its extreme past SFH (Fig. 3), it is likely that XMM-VID3-1120 also experienced a recent merger event, though further analysis of its kinematics is required to confirm this. An alternative explanation is that the starburst was the result of a significant influx of cold molecular gas, however this would require a very large gas supply for such an in-situ formation. Ex-situ growth from merger events would be more plausible (R. K. Cochrane 2025).

Unlike the others, XMM-VID3-2457 exhibits statistically different gradients (Sec. 5.1.2). It has a flat age gradient, and is very Fe-deficient in its center relative to the outskirts. Beyond the core, it has a negative [Fe/H] gradient. Like XMM-VID3-1120, it is significantly alpha-enhanced in the core ( $[\alpha/\text{Fe}] = +0.52_{-0.17}^{+0.06}$ ). This is likely caused by a massive, centrally contained starburst, enriching the core with  $\alpha$ -elements via SNe II. This could also be due to a wet merger, or accretion of cold, metal-poor gas. Both scenarios naturally explain the central Fe-deficiency by diluting the pre-existing gas. Star formation seems to have turned off uniformly, as evidenced by the flat age gradient and radial SFH, which shows that its star-formation ceased globally in a short amount of time. This is best explained by an internal mechanism, likely AGN feedback. The spectrum of XMM-VID3-2457 has evidence for an AGN, with strong [O III] $\lambda\lambda 4959, 5007$  emission, as well as emission in the H $\alpha$ + [N II] complex, potentially indicating an AGN (M. L. Hamadouche et al. 2026b). While this provides the best explanation for the observed radial gradients, we have not necessarily confirmed the presence of one; W. Chang et al. (2026) finds a relatively small AGN contribution ( $f_{\text{AGN}} = 0.16 \pm 0.11$ ) for this MQG. This does not necessarily eliminate the possibility of an AGN quenching this MQG in the past, as AGN in post-starburst galaxies have short duty cycles ( $\sim 5.3\%$ ; K. D. French et al. 2023).

Our results indicate that both uniform and rapid merger-driven quenching are already present in the first two billion years. This mirrors predictions from cosmological simulations for massive galaxies at  $z \gtrsim 3.5$  (i.e., D. Pathak et al. 2021; L. C. Kimmig et al. 2025; W. McClymont et al. 2025; P. Araya-Araya et al. 2026) and observations at lower- $z$  (i.e., M. Akhshik et al. 2023), suggesting that the diverse quenching pathways observed at low-redshift were already established in the early Universe. We present a schematic to illustrate this in Figure 7 depicting four possible quenching pathways for MQGs, as well as how such pathways would produce gradients in age, [Fe/H] and [ $\alpha$ /Fe].

From a sample size of three MQGs, we see two distinct quenching pathways; rapid, merger-driven quenching, as well as uniform quenching. This seemingly indicates that a diversity of quenching mechanisms are already operating at early times. Larger sample sizes of MQGs using spatially resolved spectroscopy are needed to confirm this.

### 5.1.4. *Comparison to Lower- $z$ Literature*

This work represents the first spatially resolved measurements of age, [Fe/H] and [ $\alpha$ /Fe] for massive qui-

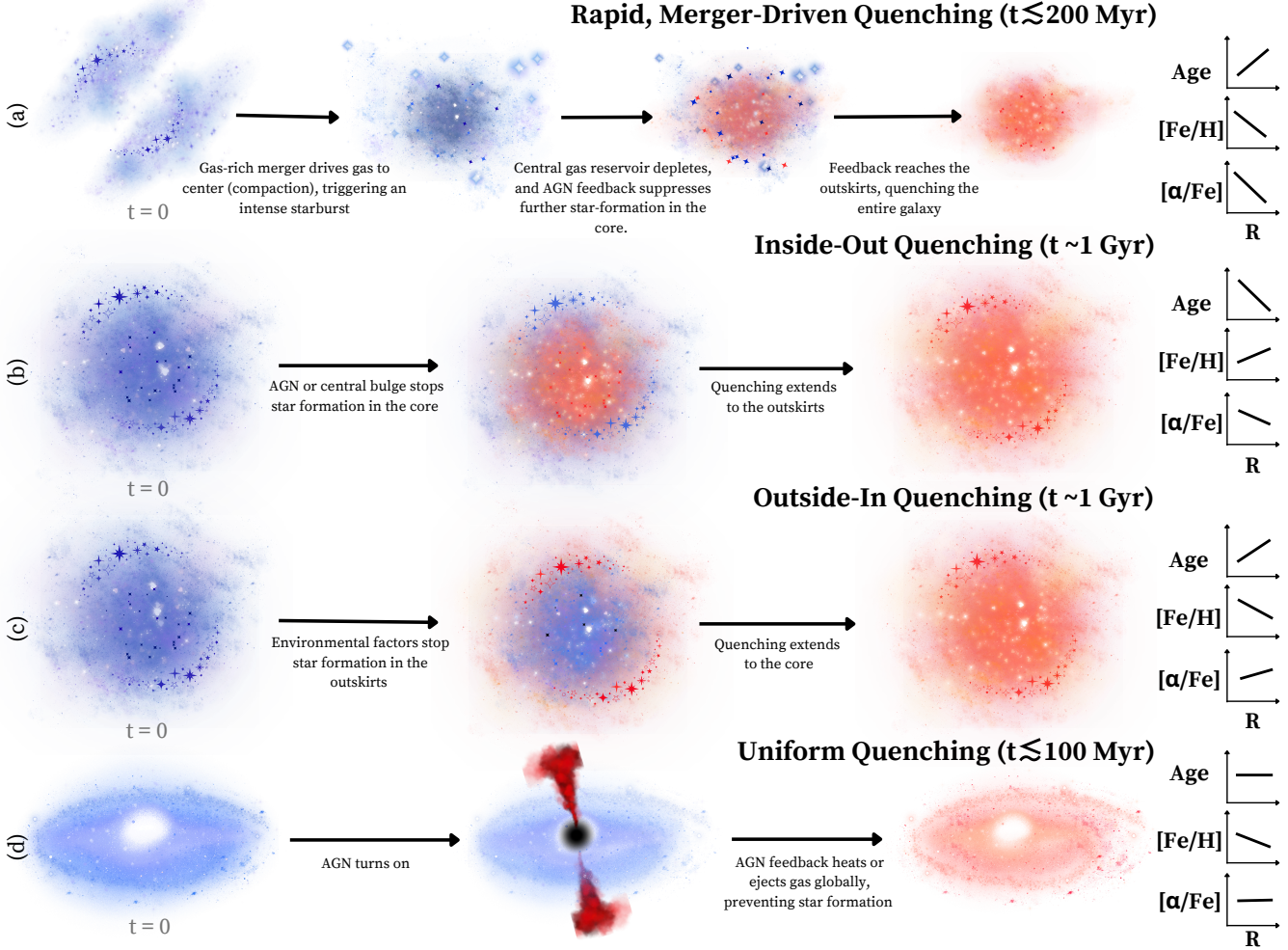


**Figure 7.** Schematic illustrating different quenching pathways possible for massive quiescent galaxies, along with the expected gradients and timescales involved. *Top row, (a):* A rapid, merger driven quenching event. The expected gradients match those observed for XMM-VID1-2075 and XMM-VID3-1120. *Upper middle row, (b):* An inside-out quenching event, where star formation in the central regions terminates first. *Lower middle row, (c):* An outside-in quenching event, where star formation in the outskirts ceases first. *Bottom row, (d):* A uniform quenching event, where an AGN quenches the host galaxy on very short timescales ( $\lesssim 100$  Myr; D. J. Setton et al. 2020; F. D’Eugenio et al. 2024), producing gradients as observed in XMM-VID3-2457.

escent galaxies at  $z \gtrsim 3$ . To frame these results in the context of the larger picture of galaxy evolution, we compare our results to lower- $z$  literature.

At  $z \sim 0.6$ , the SQuIGG $\vec{L}E$  survey found that PSB galaxies exhibit flat  $H\delta_A$  gradients (D. J. Setton et al. 2020). As  $H\delta_A$  is a proxy for stellar age, this implies that these PSBs quenched uniformly. Similar results have been shown at higher- $z$ . For example, the REQUIEM-2D survey (M. Akhshik et al. 2020, 2023) used spatially resolved HST spectroscopy to study 8 massive ( $\log_{10}(M_*/M_\odot) > 10.6$ ) quiescent galaxies at  $z \sim 2$ , finding that a subset of these MQGs have flat age gradients. Likewise, F. D’Eugenio et al. (2024) found no radial dependence in age in a massive

( $\log(M_*/M_\odot) \approx 11.2$ ) PSB galaxy at  $z \sim 3$ . These results are similar to what is found in XMM-VID3-2457, which is flat in age, and indicate that uniform quenching is common in PSBs.

In contrast, C. M. Cheng et al. (2024) studied 456 massive ( $10.3 \lesssim \log(M_*/M_\odot) \lesssim 11.8$ ) quiescent galaxies at  $0.6 \lesssim z \lesssim 1.0$  from the LEGA-C survey (A. van der Wel et al. 2016, 2021; C. M. S. Straatman et al. 2018), measuring their age,  $[Fe/H]$ , and  $[Mg/Fe]$  gradients. Over the full sample, they find flat age and  $[Mg/Fe]$  gradients, and negative  $[Fe/H]$  gradients. However, when splitting the sample into three equally sized age bins, the younger ( $1 \leq \text{age/Gyr} < 2.63$ ) subsample has a slightly positive age gradient, and negative metal-

licity gradients, as shown in Figure 5. They use this to show that these young quiescent galaxies likely underwent a merger-triggered central starburst (F. D’Eugenio et al. 2020; P.-F. Wu et al. 2020), similar to XMM-VID1-2075 and XMM-VID3-1120.

At  $z \sim 2$ , C. M. Cheng et al. (2025) measured age and abundance gradients for eight massive ( $10.3 \lesssim \log(M_*/M_\odot) \lesssim 11.1$ ) quiescent galaxies between  $1.2 \lesssim z \lesssim 2.2$  using the JWST-SUSPENSE survey (M. Slob et al. 2024). This work utilizes JWST/NIRSpec-MSA spectroscopy. To obtain ages and abundances, they also use `alf $\alpha$` , but with the C. Conroy et al. (2018) grids. They find their sample of quiescent galaxies exhibit negative age, positive [Mg/H] and [Mg/Fe], and flat [Fe/H] gradients, as depicted in Figure 5. They describe this as inside-out quenching, as the cores are older, and the low central [Mg/H] could indicate central gas expulsion (A. G. Beverage et al. 2021, 2025).

While this describes a similar quenching pattern to what is expected for our MQG sample, there is a clear difference in gradients observed between this work and C. M. Cheng et al. (2025). This is to be expected, as the galaxies studied in C. M. Cheng et al. (2025) are much older ( $\langle \text{age} \rangle \approx 2$  Gyr) than the sample studied in this work ( $\langle t_{\text{SSP}} \rangle \approx 0.6$  Gyr). This in particular is key to understanding the significantly different gradients; the older sample would have had more time to be affected by events such as minor mergers. This could lead to the negative age gradients, where the inner-most regions are left relatively untouched, while the outskirts grow over time (N. S. Haryana et al. 2025).

Furthermore, the MQGs in this work are already more massive ( $\log(M_*/M_\odot) > 11.2$ ) and more compact ( $R_e \lesssim 2$  kpc) at a higher redshift than those in C. M. Cheng et al. (2025). We highlight this in Figure 2, where we plot the stellar mass and size reported in literature of massive quiescent galaxies. Galaxies of similar mass are almost all larger in spatial extent, while similarly compact galaxies are far less massive and are observed at later epochs. It follows then that our MQGs are not evolutionarily linked to the lower- $z$  populations discussed in C. M. Cheng et al. (2025), and should perhaps be expected to undergo different processes, resulting in different gradients. This interpretation is subject to progenitor bias, as the low- $z$  quiescent population includes larger and more recently quenched galaxies, which are not represented by this compact, high- $z$  MQG sample.

## 6. CONCLUSIONS

In this work, we leverage JWST/NIRSpec IFU observations of three massive quiescent galaxies from the MAGAZ3NE survey at  $z \sim 3.5$  to measure age, [Fe/H]

and  $[\alpha/\text{Fe}]$  gradients using `alf $\alpha$`  (A. G. Beverage et al. 2025; A. Beverage 2024) with the sMILES  $\alpha$ -enhanced models (A. T. Knowles et al. 2021, 2023). We model their star-formation histories using BAGPIPES (A. C. Carnall et al. 2018, 2019) using a flexible non-parametric Gaussian Process SFH (K. G. Iyer et al. 2019) and a smooth non-parametric continuity SFH (J. Leja et al. 2019). Our main findings are summarized as follows:

- (i) All three galaxies are extremely massive ( $M_* > 10^{11.2} M_\odot$ ) with high velocity dispersions ( $\sigma_* > 325$  km/s), in agreement with previous results using Keck/MOSFIRE spectroscopy (B. Forrest et al. 2020b, 2022) (Table 1). These masses are in agreement with the most massive galaxy expected from the XMM-VIDEO survey area (Fig. 3). They are young, with mass-weighted ages  $t_{\text{MW}} \lesssim 700$  Myr and recently quenched ( $\Delta t_q = t_{\text{obs}} - t_q \approx 0.11 - 0.24$  Gyr). All three formed rapidly ( $\langle t_{\text{form}} \rangle = 422 \pm 34$  Myr) and quenched soon thereafter ( $t_q - t_{50} \lesssim 500$  Myr).
- (ii) XMM-VID1-2075 ( $[\alpha/\text{Fe}] = +0.13_{-0.08}^{+0.09}$ ) and XMM-VID3-1120 ( $[\alpha/\text{Fe}] = +0.08_{-0.20}^{+0.08}$ ) are moderately  $\alpha$ -enhanced, while XMM-VID3-2457 is consistent with a solar-scaled abundance pattern ( $[\alpha/\text{Fe}] = -0.02_{-0.05}^{+0.05}$ ) (Table 2). This is somewhat surprising, as massive quiescent galaxies observed at high- $z$  are commonly  $\alpha$ -enhanced ( $[\alpha/\text{Fe}] \gtrsim +0.3$ ; i.e., M. Kriek et al. 2016; A. G. Beverage et al. 2025; L. C. Kimmig et al. 2025). However, a spread in  $\alpha$ -enhancement has been observed ( $\langle [\alpha/\text{Fe}] \rangle = +0.22_{-0.17}^{+0.22}$ ; M. L. Hamadouche et al. 2026b), reflecting a diversity in evolutionary paths. This work adds to the body of literature that shows this diversity.
- (iii) The central regions of the three MQGs are remarkably similar, with young ( $\langle t_{\text{SSP}} \rangle \approx 0.6$  Gyr) ages, elevated ( $\gtrsim +0.21$ )  $[\alpha/\text{Fe}]$ , and solar metallicities ( $[\text{Fe}/\text{H}] \approx 0$ ) for two of the MQGs (Fig. 4). This is consistent with a recent, intense starburst. This is supported by the SFHs, which show a large burst ( $\text{SFR}_{\text{peak}} \approx 500 M_\odot \text{yr}^{-1}$ ) of star-formation between  $4 < z < 5$  (Fig. 3). The radial SFHs agree with this picture, with central surface SFR densities that peak above  $\Sigma_{\text{SFR}} > 50 M_\odot \text{yr}^{-1} \text{kpc}^{-2}$ . This large burst is consistent with a previous submillimeter galaxy phase, which are commonly considered a plausible progenitor to MQGs.
- (iv) We find that both XMM-VID1-2075 and XMM-VID3-1120 have statistically similar age and [Fe/H] gradients, while XMM-VID3-2457 exhibits

statistically different age, [Fe/H] and  $[\alpha/\text{Fe}]$  gradients than the other two galaxies. In particular, both XMM-VID1-2075 and XMM-VID3-1120 exhibit positive age gradients and negative  $[\alpha/\text{Fe}]$  gradients (Fig. 4), consistent with a rapid, merger-driven quenching event (Fig. 7).

- (v) XMM-VID3-2457 exhibits a flat age gradient (Fig. 4), suggestive of uniform quenching. Furthermore, its core is significantly  $\alpha$ -enhanced ( $[\alpha/\text{Fe}] = +0.52^{+0.06}_{-0.17}$ ) and Fe-deficient ( $[\text{Fe}/\text{H}] = -0.42^{+0.21}_{-0.14}$ ). This galaxy was quenched uniformly on very short ( $\Delta t_q \lesssim 100$  Myr) timescales (Figures 4, 6). Internal mechanisms are the most likely cause for quenching. The spectrum provides some evidence for an AGN, with [O III] emission ( $\text{EW}_{\text{rest}} = 3.6 \text{ \AA}$ ) and [N II] emission ( $\text{EW}_{\text{rest}} = 3.5 \text{ \AA}$ ).
- (vi) A significant discrepancy ( $\approx 0.2-0.4$  dex) appears between the reported metallicities from BAGPIPES ( $\langle \log_{10}(Z/Z_{\odot}) \rangle = 0.31$ ) and  $\text{alf}\alpha$  ( $\langle [\text{Fe}/\text{H}] \rangle = 0.02$ ) (Tables 1 & 2). This is similar to other recent results showing that the metallicity measurements between codes using solar-scaled versus  $\alpha$ -enhanced models differ significantly (A. G. Beverage et al. 2025; I. McConachie et al. 2025a; H.-H. Leung et al. 2026b). We note, however, that BAGPIPES mass-weighted ages and  $\text{alf}\alpha$  SSP-equivalent ages agree within  $\approx 1\sigma$ . This offset in inferred metallicities impacts all analyses of the star formation histories of high- $z$  quiescent galax-

ies, and future work is required to further investigate this.

This work presents the first spatially resolved analysis of stellar population gradients of massive quiescent galaxies in the first 2 Gyr of cosmic time. Despite our small sample size, these results highlight the importance of spatially resolved spectroscopy and  $\alpha$ -enhancement consideration in probing massive galaxy formation in the early Universe.

## ACKNOWLEDGMENTS

We thank Chloe Cheng for providing LEGA-C data. We also thank Kartheik Iyer for discussions on how to use the flexible non-parametric GP-SFH models. JAD acknowledges funding from the Dunlap Institute, made possible through an endowment established by the David Dunlap family and the University of Toronto. AM acknowledges support from the Yavin Family Fund. BF acknowledges support from JWST-GO-02913.001-A. DM acknowledges generous support from the Leonard and Jane Holmes Bernstein Professorship in Evolutionary Science. GW gratefully acknowledges support from the National Science Foundation through grant AST-2347348.

*Facilities:* JWST

*Software:* `astropy` (Astropy Collaboration et al. 2022), `alfalpha` (A. Beverage 2024; A. G. Beverage et al. 2025), BAGPIPES (A. C. Carnall et al. 2018, 2019), `statsmodels` (S. Skipper & P. Josef 2010)

## APPENDIX

### A. SPECTRA

#### B. TABLES

##### B.1. *Fitting Priors*

##### B.2. *Fitting Results*

### C. ALF $\alpha$ TESTING

We compare the sMILES and MILES+IRTF (C. Conroy et al. 2018) grids in order to understand the systemic differences between these two stellar population models. We do this by creating a mock galaxy spectrum using BAGPIPES, and then running it through  $\text{alf}\alpha$  with both grids. This allows us to set the age, metallicity and  $[\alpha/\text{Fe}]$  as a known prior, therefore allowing us to directly compare our ability to recover these parameters using each of these models. We create a mock galaxy spectrum at  $z = 2$ , with age ( $t_{\text{age}} = 1.1$  Gyr), solar metallicity ( $Z_* = Z_{\odot}$ ), and velocity dispersion ( $\sigma_* = 200$  km/s). BAGPIPES uses BC03, which is solar-scaled,  $[\alpha/\text{Fe}] = 0$  by default. All specified values are within the constraints of both the sMILES and C. Conroy et al. (2018) grids. We use an exponential star formation history with  $\tau = 0.05$  Gyr. This is chosen to resemble how  $\text{alf}\alpha$  models the SFH, which assumes a single burst. Finally, we add noise to the spectrum, resulting in a signal-to-noise  $\approx 20 \text{ \AA}^{-1}$  spectrum.

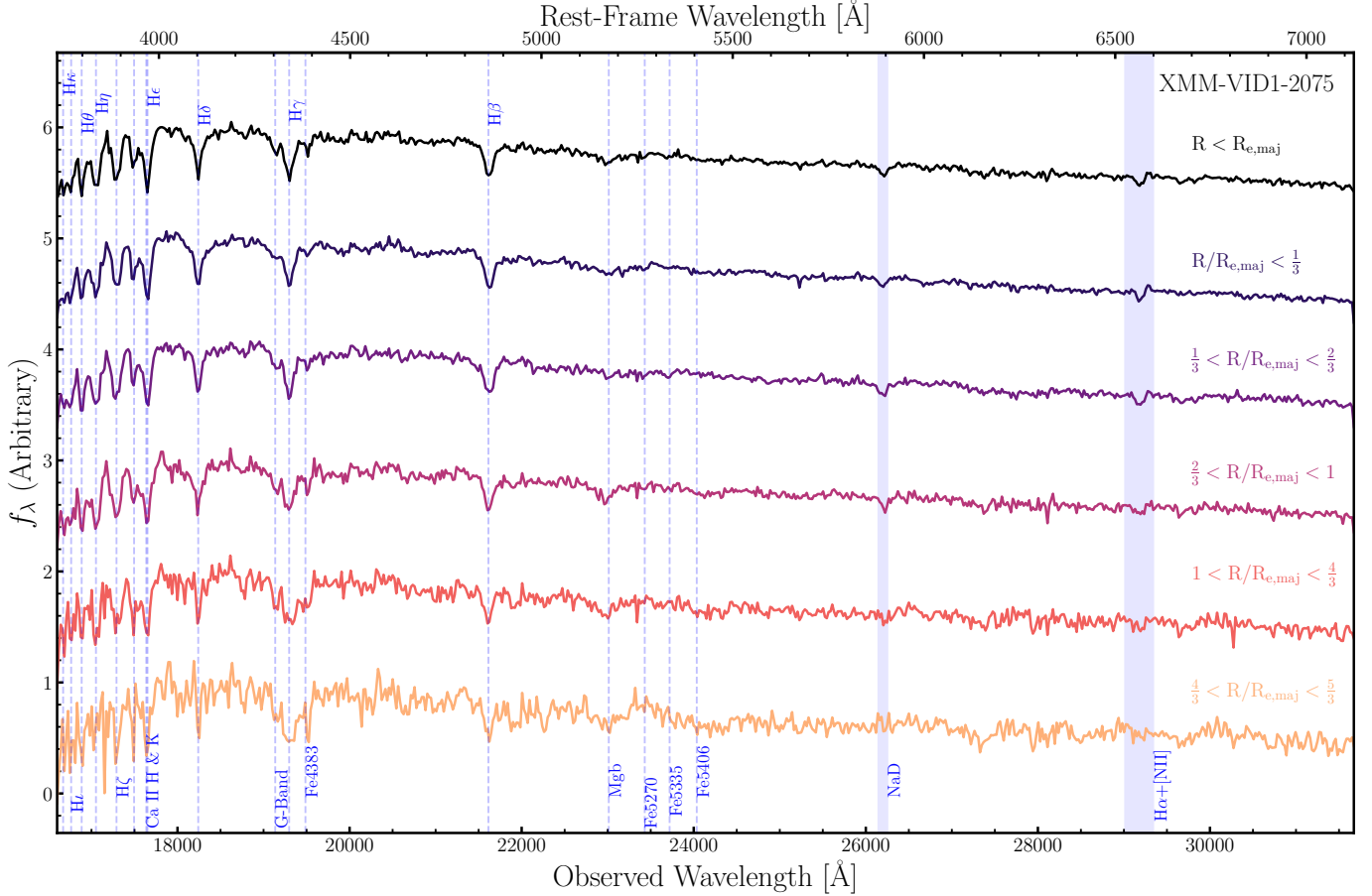


**Figure 8.** Extracted spectra for XMM-VID1-2075, within  $R < R_e$  (top, black) and elliptical radial bins, normalized and scaled arbitrarily for visual purposes.

We show the results of this testing in Fig. 11 by plotting the posterior distributions of age ( $t_{\text{age}}$ ),  $[\text{Fe}/\text{H}]$ ,  $[\text{Z}/\text{H}]$ , and  $[\alpha/\text{Fe}]$  for both the sMILES models as well as the MILES+IRTF models from C. Conroy et al. (2018) as 1-D histograms. The input parameter values for the mock galaxy are shown as a dashed black line. sMILES better recovers total metallicity and age (top and bottom left panels, respectively) than the MILES+IRTF models, capturing the input parameters within  $1\sigma$ . However, this is not true for  $[\text{Fe}/\text{H}]$  and  $[\alpha/\text{Fe}]$ . Although the input spectrum assumes a solar metallicity ( $[\text{Fe}/\text{H}] = 0$ ), neither sMILES nor the MILES+IRTF model recovers this, returning values of  $[\text{Fe}/\text{H}] = -0.071^{+0.004}_{-0.004}$  and  $[\text{Fe}/\text{H}] = -0.028^{+0.007}_{-0.006}$  respectively. Furthermore, sMILES struggles with recovering  $[\alpha/\text{Fe}]$ , returning  $[\alpha/\text{Fe}] = +0.106^{+0.003}_{-0.003}$ , while MILES+IRTF returns  $[\alpha/\text{Fe}] = +0.001^{+0.007}_{-0.008}$ , consistent with the input value of 0 from Bagpipes. This offset of  $\approx 0.1$  dex in both  $[\text{Fe}/\text{H}]$  and  $[\alpha/\text{Fe}]$  reflects important differences between the underlying stellar population models.

To understand the cause of this offset, we create model spectra using the MILES+IRTF and sMILES grids that have similar parameters as the BAGPIPES mock galaxy spectrum. We show these model spectra in Figure 12. The spectra of all three models appears largely similar. However, they differ non-trivially, particularly at Balmer absorption line depths. This should be expected, as the model spectra are made from SSPs that use different isochrones and stellar libraries. We discuss this more in Section C.1.

### C.1. Effects of different Isochrones & Stellar Libraries

Two stellar population synthesis (SPS) codes applied to the same spectrum can reasonably return different parameters due to differences in the isochrones and stellar libraries. Previous literature has studied such systematic offsets when observing local galaxies. R. Asa'd & P. Goudfrooij (2020) found that for galaxies aged  $\sim 2$ -5 Gyr, the age measured using MIST (J. Choi et al. 2016) isochrones is always  $+0.2$  dex above the age measured using Padova (M. R. L. Cioni et al. 2006a,b) isochrones even when using the wavelength range of 3700 Å to 5000 Å. D. B. Palakkatharappil &





Component	Parameter	Range	Prior
<b>Global</b>			
	Redshift	$(z_{\text{spec}} - 0.1, z_{\text{spec}} + 0.1)$	Uniform
	Velocity Dispersion ( $\sigma_*$ , km s <sup>-1</sup> )	(300, 600)	Gaussian ( $\mu = 400, \sigma = 25$ )
<b>Iyer et al. (2019) Non-parametric SFH</b>			
	SFR ( $M_{\odot}$ yr <sup>-1</sup> )	$(1 \times 10^{-8}, 2 \times 10^4)$	log <sub>10</sub>
	Bins	10	–
	Bins_prior	–	Dirichlet
	$t_x$	[10, 20, 30, 40, 50, 60, 70, 80, 90]	–
	$\alpha$	[30, 3, 3, 3, 3, 3, 3, 3, 3]	–
	Stellar Mass ( $\log(M_*/M_{\odot})$ )	(6, 13)	Uniform
	Metallicity ( $Z_{\odot}$ )	(0.01, 5)	log <sub>10</sub>
<b>Continuity (Leja et al. 2019) Non-parametric SFH</b>			
	Bins	10	–
	$\log_{10}(\text{SFR}_i/\text{SFR}_{i+1})$	(-100, 100)	Student- $t$ ( $\sigma = 0.7, \nu = 2$ )
	Stellar Mass ( $\log(M_*/M_{\odot})$ )	(6, 13)	Uniform
	Metallicity ( $Z_{\odot}$ )	(0.01, 5)	log <sub>10</sub>
<b>Dust</b>			
	Type	Calzetti	–
	$A_v$	(0, 1)	Uniform
<b>Noise</b>			
	Type	Gaussian Process (SHOTerm)	–
	White noise scaling ( $s$ )	(1, 10)	log <sub>10</sub>
	Correlated amplitude ( $\sigma$ )	$(1 \times 10^{-4}, 1 \times 10^{-1})$	log <sub>10</sub>
	Period/length scale ( $\rho$ )	$(1 \times 10^{-5}, 1)$	log <sub>10</sub>
	Dampening Quality Factor ( $Q$ )	0.49	Fixed
<b>Nebular</b>			
	Ionization Parameter ( $\log_{10}(U)$ )	(-2, -4)	Uniform
<b>AGN component<sup>a</sup></b>			
	$f_{\text{H}\alpha, \text{broad}}$ (erg s <sup>-1</sup> cm <sup>-2</sup> )	$(0, 2.5 \times 10^{-17})$	Uniform
	$f_{5100}$ (erg s <sup>-1</sup> cm <sup>-2</sup> Å <sup>-1</sup> )	$(0, 1 \times 10^{-19})$	Uniform
	$\sigma_{\text{AGN}}$ (km s <sup>-1</sup> )	(1000, 7000)	log <sub>10</sub>
	$\alpha_{\lambda < 5000\text{\AA}}$	(-2, 4)	Gaussian ( $\mu = -1.5, \sigma = 0.5$ )
	$\alpha_{\lambda > 5000\text{\AA}}$	(-2, 2)	Gaussian ( $\mu = 0.5, \sigma = 0.5$ )

<sup>a</sup>Only for XMM-VID3-2457.**Table 3.** Priors used in BAGPIPES spectral fitting.

- Asplund, M., Grevesse, N., & Sauval, A. J. 2005, in *Astronomical Society of the Pacific Conference Series*, Vol. 336, *Cosmic Abundances as Records of Stellar Evolution and Nucleosynthesis*, ed. T. G. Barnes, III & F. N. Bash, 25
- Astropy Collaboration, Price-Whelan, A. M., Lim, P. L., et al. 2022, *ApJ*, 935, 167, doi: [10.3847/1538-4357/ac7c74](https://doi.org/10.3847/1538-4357/ac7c74)
- Baker, W. M., Valentino, F., Lagos, C. d. P., et al. 2025, *A&A*, 702, A270, doi: [10.1051/0004-6361/202555829](https://doi.org/10.1051/0004-6361/202555829)
- Belli, S., Newman, A. B., & Ellis, R. S. 2014, *ApJ*, 783, 117, doi: [10.1088/0004-637X/783/2/117](https://doi.org/10.1088/0004-637X/783/2/117)
- Belli, S., Newman, A. B., & Ellis, R. S. 2015, *ApJ*, 799, 206, doi: [10.1088/0004-637X/799/2/206](https://doi.org/10.1088/0004-637X/799/2/206)
- Belli, S., Newman, A. B., & Ellis, R. S. 2019, *ApJ*, 874, 17, doi: [10.3847/1538-4357/ab07af](https://doi.org/10.3847/1538-4357/ab07af)
- Belli, S., Genzel, R., Förster Schreiber, N. M., et al. 2017, *ApJL*, 841, L6, doi: [10.3847/2041-8213/aa70e5](https://doi.org/10.3847/2041-8213/aa70e5)

Parameter	Prior Range
Age (Gyr)	$(10^{-1.5}, t_H(z))$
$\sigma_*$ (km s <sup>-1</sup> )	(100, 500)
Recessional Velocity (km/s)	(-500, 500)
Metallicity [Z/H]	(-1.5, 0.26)
[ $\alpha$ /Fe]	(-0.2, +0.6)
Jitter	(0.1, 10)

**Table 4.** Prior ranges for the `alf $\alpha$`  fits. The upper bound of the age parameter is determined by calculating for the age of the Universe at the redshift of the galaxy.

- Beverage, A. 2024, `alizabeverage/alfalpha`: Initial Release alongside Beverage et al. 2024, v1.0.0 Zenodo, doi: [10.5281/zenodo.13882666](https://doi.org/10.5281/zenodo.13882666)
- Beverage, A. G., Kriek, M., Conroy, C., et al. 2021, *ApJL*, 917, L1, doi: [10.3847/2041-8213/ac12cd](https://doi.org/10.3847/2041-8213/ac12cd)
- Beverage, A. G., Kriek, M., Suess, K. A., et al. 2024, *ApJ*, 966, 234, doi: [10.3847/1538-4357/ad372d](https://doi.org/10.3847/1538-4357/ad372d)
- Beverage, A. G., Slob, M., Kriek, M., et al. 2025, *ApJ*, 979, 249, doi: [10.3847/1538-4357/ad96b6](https://doi.org/10.3847/1538-4357/ad96b6)
- Bezanson, R., van Dokkum, P. G., Tal, T., et al. 2009, *ApJ*, 697, 1290, doi: [10.1088/0004-637X/697/2/1290](https://doi.org/10.1088/0004-637X/697/2/1290)
- Böker, T., Arribas, S., Lützgendorf, N., et al. 2022, *A&A*, 661, A82, doi: [10.1051/0004-6361/202142589](https://doi.org/10.1051/0004-6361/202142589)
- Brammer, G. B., Whitaker, K. E., van Dokkum, P. G., et al. 2011, *ApJ*, 739, 24, doi: [10.1088/0004-637X/739/1/24](https://doi.org/10.1088/0004-637X/739/1/24)
- Bruzual, G., & Charlot, S. 2003, *MNRAS*, 344, 1000, doi: [10.1046/j.1365-8711.2003.06897.x](https://doi.org/10.1046/j.1365-8711.2003.06897.x)
- Bushouse, H., Eisenhamer, J., Dencheva, N., et al. 2025, JWST Calibration Pipeline, 1.19.1 Zenodo, doi: [10.5281/zenodo.6984365](https://doi.org/10.5281/zenodo.6984365)
- Calzetti, D., Armus, L., Bohlin, R. C., et al. 2000, *ApJ*, 533, 682, doi: [10.1086/308692](https://doi.org/10.1086/308692)
- Carnall, A. C., McLure, R. J., Dunlop, J. S., & Davé, R. 2018, *MNRAS*, 480, 4379, doi: [10.1093/mnras/sty2169](https://doi.org/10.1093/mnras/sty2169)
- Carnall, A. C., McLure, R. J., Dunlop, J. S., et al. 2019, *MNRAS*, 490, 417, doi: [10.1093/mnras/stz2544](https://doi.org/10.1093/mnras/stz2544)
- Carnall, A. C., McLure, R. J., Dunlop, J. S., et al. 2023a, *Nature*, 619, 716, doi: [10.1038/s41586-023-06158-6](https://doi.org/10.1038/s41586-023-06158-6)
- Carnall, A. C., McLeod, D. J., McLure, R. J., et al. 2023b, *MNRAS*, 520, 3974, doi: [10.1093/mnras/stad369](https://doi.org/10.1093/mnras/stad369)
- Carnall, A. C., Cullen, F., McLure, R. J., et al. 2024, *MNRAS*, 534, 325, doi: [10.1093/mnras/stae2092](https://doi.org/10.1093/mnras/stae2092)
- Chabrier, G. 2003, *PASP*, 115, 763, doi: [10.1086/376392](https://doi.org/10.1086/376392)
- Chang, W., Wilson, G., Forrest, B., et al. 2026, arXiv e-prints, arXiv:2601.22844, doi: [10.48550/arXiv.2601.22844](https://doi.org/10.48550/arXiv.2601.22844)
- Cheng, C. M., Kriek, M., Beverage, A. G., et al. 2024, *MNRAS*, 532, 3604, doi: [10.1093/mnras/stae1739](https://doi.org/10.1093/mnras/stae1739)
- Cheng, C. M., Slob, M., Kriek, M., et al. 2025, arXiv e-prints, arXiv:2509.12316, doi: [10.48550/arXiv.2509.12316](https://doi.org/10.48550/arXiv.2509.12316)
- Cheng, C. M., Slob, M., Kriek, M., et al. 2026, arXiv e-prints, arXiv:2601.20864, doi: [10.48550/arXiv.2601.20864](https://doi.org/10.48550/arXiv.2601.20864)
- Choi, J., Dotter, A., Conroy, C., et al. 2016, *ApJ*, 823, 102, doi: [10.3847/0004-637X/823/2/102](https://doi.org/10.3847/0004-637X/823/2/102)
- Cioni, M. R. L., Girardi, L., Marigo, P., & Habing, H. J. 2006a, *A&A*, 448, 77, doi: [10.1051/0004-6361:20053933](https://doi.org/10.1051/0004-6361:20053933)
- Cioni, M. R. L., Girardi, L., Marigo, P., & Habing, H. J. 2006b, *A&A*, 452, 195, doi: [10.1051/0004-6361:20054699](https://doi.org/10.1051/0004-6361:20054699)
- Cochrane, R. K. 2025, *MNRAS*, 544, 1530, doi: [10.1093/mnras/staf1568](https://doi.org/10.1093/mnras/staf1568)
- Conroy, C., & van Dokkum, P. G. 2012, *ApJ*, 760, 71, doi: [10.1088/0004-637X/760/1/71](https://doi.org/10.1088/0004-637X/760/1/71)
- Conroy, C., Villaume, A., van Dokkum, P. G., & Lind, K. 2018, *ApJ*, 854, 139, doi: [10.3847/1538-4357/aaab49](https://doi.org/10.3847/1538-4357/aaab49)
- Daddi, E., Renzini, A., Pirzkal, N., et al. 2005, *ApJ*, 626, 680, doi: [10.1086/430104](https://doi.org/10.1086/430104)
- de Graaff, A., Bezanson, R., Franx, M., et al. 2021, *ApJ*, 913, 103, doi: [10.3847/1538-4357/abf1e7](https://doi.org/10.3847/1538-4357/abf1e7)
- de Graaff, A., Setton, D. J., Brammer, G., et al. 2025, *Nature Astronomy*, 9, 280, doi: [10.1038/s41550-024-02424-3](https://doi.org/10.1038/s41550-024-02424-3)
- De Lucia, G., Tornatore, L., Frenk, C. S., et al. 2014, *MNRAS*, 445, 970, doi: [10.1093/mnras/stu1752](https://doi.org/10.1093/mnras/stu1752)
- D’Eugenio, F., van der Wel, A., Wu, P.-F., et al. 2020, *MNRAS*, 497, 389, doi: [10.1093/mnras/staa1937](https://doi.org/10.1093/mnras/staa1937)
- D’Eugenio, F., Pérez-González, P. G., Maiolino, R., et al. 2024, *Nature Astronomy*, 8, 1443, doi: [10.1038/s41550-024-02345-1](https://doi.org/10.1038/s41550-024-02345-1)
- Dunlop, J., Peacock, J., Spinrad, H., et al. 1996, *Nature*, 381, 581, doi: [10.1038/381581a0](https://doi.org/10.1038/381581a0)
- Falcón-Barroso, J., Sánchez-Blázquez, P., Vazdekis, A., et al. 2011, *A&A*, 532, A95, doi: [10.1051/0004-6361/201116842](https://doi.org/10.1051/0004-6361/201116842)
- Foreman-Mackey, D. 2018, *Research Notes of the American Astronomical Society*, 2, 31, doi: [10.3847/2515-5172/aaaff6c](https://doi.org/10.3847/2515-5172/aaaff6c)

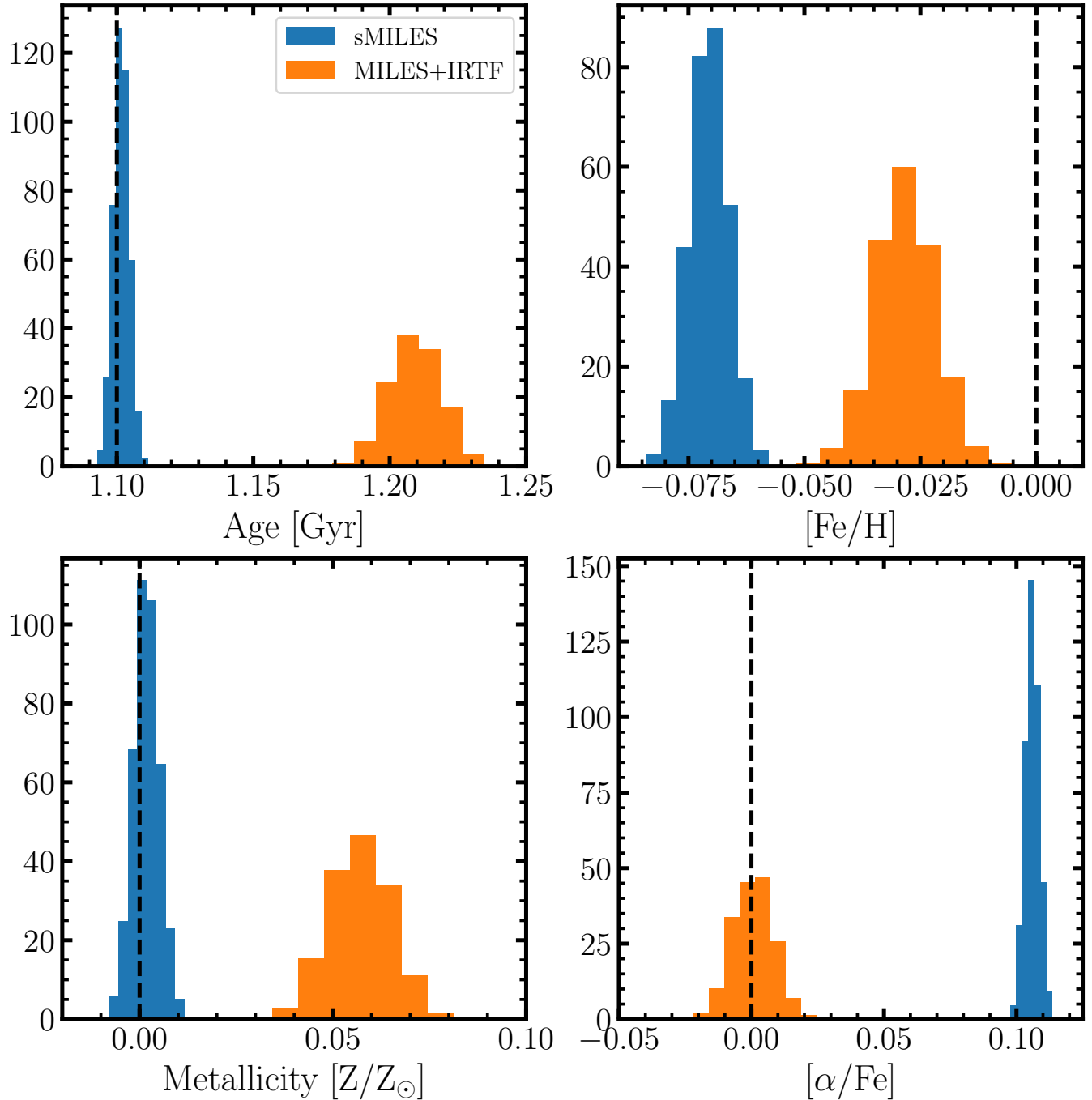


**Figure 11.** Results from fitting a model galaxy made in BAGPIPES with `alf $\alpha$` , using the MILES+IRTF models from C. Conroy et al. (2018) (orange) and sMILES (A. T. Knowles et al. 2023) (blue) for age (top left), [Fe/H] (top right), metallicity (bottom left), and [α/Fe] (bottom right). Posterior fitting distributions are presented as probability density functions. The model galaxy is made with an age of 1.1 Gyr,  $Z_* = Z_\odot$ , [α/Fe] = 0, and  $\sigma_* = 200$  km/s. These values are indicated by a black dashed line.

Foreman-Mackey, D., Agol, E., Ambikasaran, S., & Angus,

R. 2017, AJ, 154, 220, doi: [10.3847/1538-3881/aa9332](https://doi.org/10.3847/1538-3881/aa9332)

Foreman-Mackey, D., Hogg, D. W., Lang, D., & Goodman,

J. 2013, PASP, 125, 306, doi: [10.1086/670067](https://doi.org/10.1086/670067)

Forrest, B., Annunziatella, M., Wilson, G., et al. 2020a,

ApJL, 890, L1, doi: [10.3847/2041-8213/ab5b9f](https://doi.org/10.3847/2041-8213/ab5b9f)

Forrest, B., Marsan, Z. C., Annunziatella, M., et al. 2020b,

ApJ, 903, 47, doi: [10.3847/1538-4357/abb819](https://doi.org/10.3847/1538-4357/abb819)

Forrest, B., Wilson, G., Muzzin, A., et al. 2022, ApJ, 938,

109, doi: [10.3847/1538-4357/ac8747](https://doi.org/10.3847/1538-4357/ac8747)

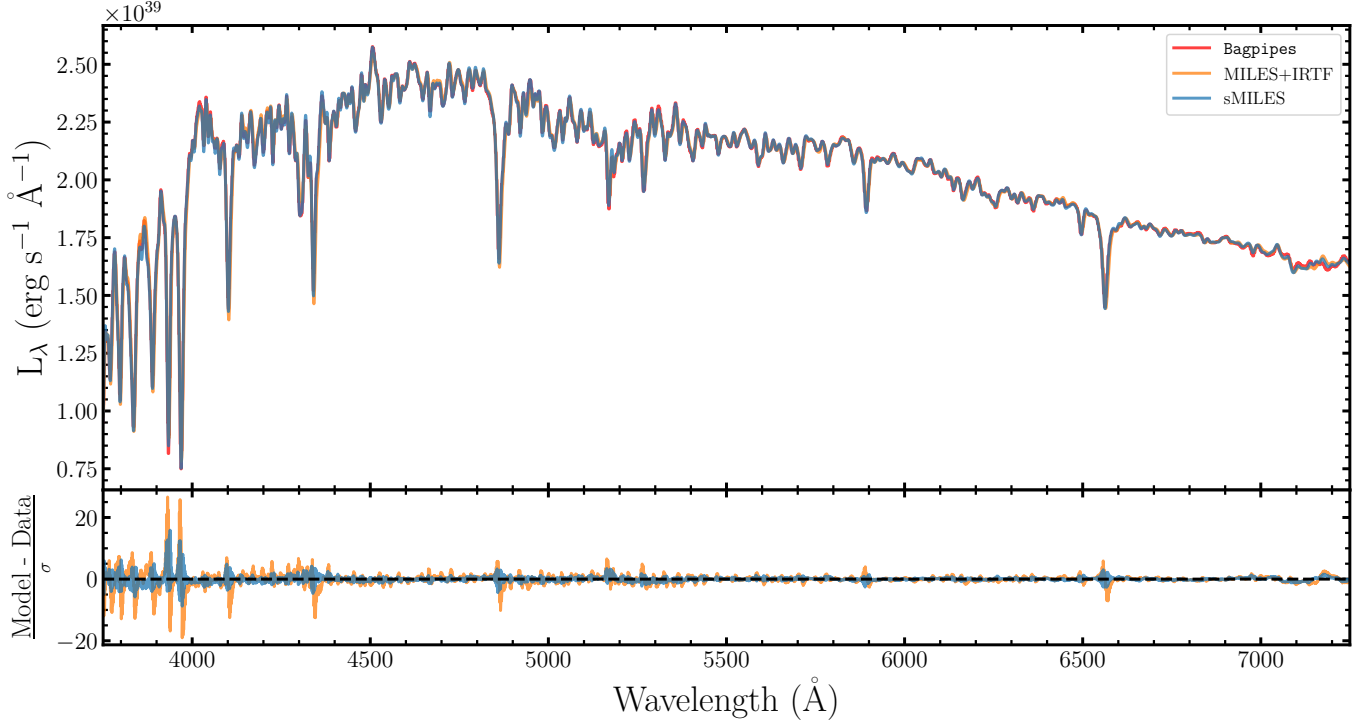


**Figure 12.** *Top:* Red: BAGPIPES model spectrum of a 1.1 Gyr galaxy with  $Z_* = Z_\odot$ ,  $[\alpha/\text{Fe}] = 0$ , and  $\sigma_* = 200$  km/s. MILES+IRTF (orange) and sMILES (blue) fits from `alf $\alpha$` . *Bottom:* The residuals between the MILES+IRTF and sMILES fits and the model galaxy. Significant differences between the models are seen, particularly for Balmer absorption line depths. The MILES+IRTF spectrum has deeper Balmer lines than either sMILES or BAGPIPES.

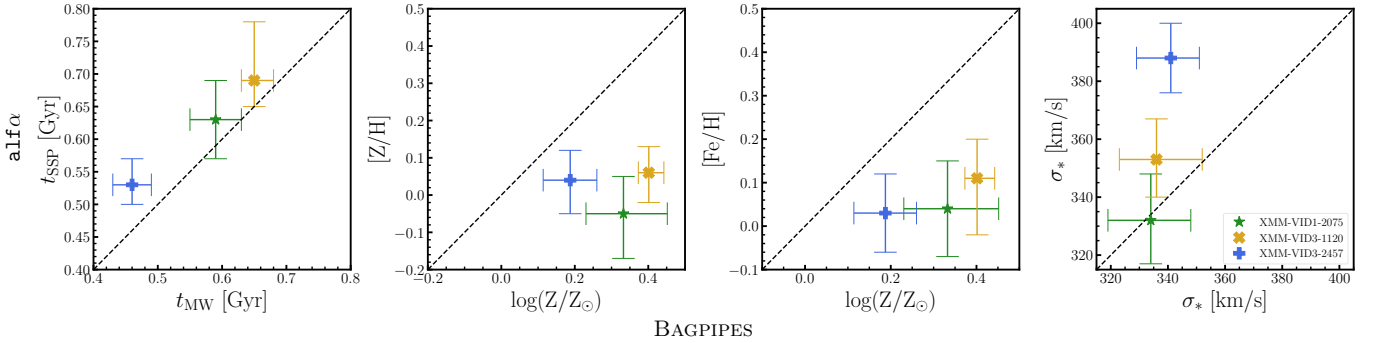


**Figure 13.** A comparison of different stellar population parameters inferred from `alf $\alpha$`  (y-axis) and BAGPIPES (x-axis) for our integrated spectra ( $R < R_e$ ). The one-to-one line is indicated as a black dashed line. *Left:* SSP-equivalent ages from `alf $\alpha$`  compared to the mass-weighted ages from BAGPIPES. *Center-left:*  $[Z/H]$  inferred from `alf $\alpha$`  versus  $\log(Z_*/Z_\odot)$  from BAGPIPES. *Center-right:*  $[\text{Fe}/H]$  versus  $\log(Z_*/Z_\odot)$  for the three galaxies. *Right:* A comparison of velocity dispersions  $\sigma_*$  measured from `alf $\alpha$`  and BAGPIPES. Both take into account the wavelength dependent nature of the JWST/NIRSpec IFU instrumental dispersion.

Forrest, B., Annunziatella, M., Chang, W., et al. 2023, Dissecting the Monsters: Resolved IFU Spectroscopy of the Most Massive Quiescent Galaxies at  $z > 3$ , JWST Proposal. Cycle 2, ID. #2913

Forrest, B., Cooper, M. C., Muzzin, A., et al. 2024, ApJ, 977, 51, doi: [10.3847/1538-4357/ad8b1c](https://doi.org/10.3847/1538-4357/ad8b1c)

Forrest, B., Muzzin, A., Marchesini, D., et al. 2026, Nature Astronomy, doi: [10.1038/s41550-026-02855-0](https://doi.org/10.1038/s41550-026-02855-0)

French, K. D., Earl, N., Novack, A. B., et al. 2023, ApJ, 950, 153, doi: [10.3847/1538-4357/acd249](https://doi.org/10.3847/1538-4357/acd249)

García-Benito, R., González Delgado, R. M., Pérez, E., et al. 2017, A&A, 608, A27, doi: [10.1051/0004-6361/201731357](https://doi.org/10.1051/0004-6361/201731357)

Glazebrook, K., Abraham, R. G., McCarthy, P. J., et al. 2004, Nature, 430, 181, doi: [10.1038/nature02667](https://doi.org/10.1038/nature02667)

- Glazebrook, K., Schreiber, C., Labbé, I., et al. 2017, *Nature*, 544, 71, doi: [10.1038/nature21680](https://doi.org/10.1038/nature21680)
- Glazebrook, K., Nanayakkara, T., Schreiber, C., et al. 2024, *Nature*, 628, 277, doi: [10.1038/s41586-024-07191-9](https://doi.org/10.1038/s41586-024-07191-9)
- Gómez-Guijarro, C., Toft, S., Karim, A., et al. 2018, *ApJ*, 856, 121, doi: [10.3847/1538-4357/aab206](https://doi.org/10.3847/1538-4357/aab206)
- Gountanis, N. M., Weinberg, D. H., Beverage, A. G., et al. 2025, *ApJ*, 985, 184, doi: [10.3847/1538-4357/adc4e6](https://doi.org/10.3847/1538-4357/adc4e6)
- Grevesse, N., & Noels, A. 1993, in *Origin and Evolution of the Elements*, ed. N. Prantzos, E. Vangioni-Flam, & M. Casse, 15–25
- Hamadouche, M. L., Antwi-Danso, J., Beverage, A., & Whitaker, K. E. 2026a, arXiv e-prints, arXiv:2603.13479, doi: [10.48550/arXiv.2603.13479](https://doi.org/10.48550/arXiv.2603.13479)
- Hamadouche, M. L., Whitaker, K. E., Valentino, F., et al. 2026b, arXiv e-prints, arXiv:2602.02485, doi: [10.48550/arXiv.2602.02485](https://doi.org/10.48550/arXiv.2602.02485)
- Haryana, N. S., Akiyama, M., Abdurro'uf, et al. 2025, *ApJ*, 994, 215, doi: [10.3847/1538-4357/ae03ad](https://doi.org/10.3847/1538-4357/ae03ad)
- Hopkins, P. F., Murray, N., Quataert, E., & Thompson, T. A. 2010, *MNRAS*, 401, L19, doi: [10.1111/j.1745-3933.2009.00777.x](https://doi.org/10.1111/j.1745-3933.2009.00777.x)
- Ito, K., Valentino, F., Farcy, M., et al. 2025, *A&A*, 697, A111, doi: [10.1051/0004-6361/202453211](https://doi.org/10.1051/0004-6361/202453211)
- Iyer, K. G., Gawiser, E., Faber, S. M., et al. 2019, *ApJ*, 879, 116, doi: [10.3847/1538-4357/ab2052](https://doi.org/10.3847/1538-4357/ab2052)
- Jafariyazani, M., Newman, A. B., Mobasher, B., et al. 2025, *ApJ*, 986, 148, doi: [10.3847/1538-4357/addbdc](https://doi.org/10.3847/1538-4357/addbdc)
- Jafariyazani, M., Newman, A. B., Mobasher, B., et al. 2020, *ApJL*, 897, L42, doi: [10.3847/2041-8213/aba11c](https://doi.org/10.3847/2041-8213/aba11c)
- Ji, Z., Williams, C. C., Behroozi, P., et al. 2026, arXiv e-prints, arXiv:2604.05022, doi: [10.48550/arXiv.2604.05022](https://doi.org/10.48550/arXiv.2604.05022)
- Johnson, B. D., Leja, J., Conroy, C., & Speagle, J. S. 2021, *ApJS*, 254, 22, doi: [10.3847/1538-4365/abef67](https://doi.org/10.3847/1538-4365/abef67)
- Jones, A. P., & Nuth, J. A. 2011, *A&A*, 530, A44, doi: [10.1051/0004-6361/201014440](https://doi.org/10.1051/0004-6361/201014440)
- Kass, R. E., & Raftery, A. E. 1995, *J. Am. Statist. Assoc.*, 90, 773, doi: [10.1080/01621459.1995.10476572](https://doi.org/10.1080/01621459.1995.10476572)
- Kawinwanichakij, L., Glazebrook, K., Nanayakkara, T., et al. 2026, *ApJ*, 997, 29, doi: [10.3847/1538-4357/ae0a18](https://doi.org/10.3847/1538-4357/ae0a18)
- Keating, S. K., Abraham, R. G., Schiavon, R., et al. 2015, *ApJ*, 798, 26, doi: [10.1088/0004-637X/798/1/26](https://doi.org/10.1088/0004-637X/798/1/26)
- Kimmig, L. C., Remus, R.-S., Seidel, B., et al. 2025, *ApJ*, 979, 15, doi: [10.3847/1538-4357/ad9472](https://doi.org/10.3847/1538-4357/ad9472)
- Knowles, A. T., Sansom, A. E., Allende Prieto, C., & Vazdekis, A. 2021, *MNRAS*, 504, 2286, doi: [10.1093/mnras/stab1001](https://doi.org/10.1093/mnras/stab1001)
- Knowles, A. T., Sansom, A. E., Vazdekis, A., & Allende Prieto, C. 2023, *MNRAS*, 523, 3450, doi: [10.1093/mnras/stad1647](https://doi.org/10.1093/mnras/stad1647)
- Kobayashi, C., & Nomoto, K. 2009, *ApJ*, 707, 1466, doi: [10.1088/0004-637X/707/2/1466](https://doi.org/10.1088/0004-637X/707/2/1466)
- Kriek, M., van der Wel, A., van Dokkum, P. G., Franx, M., & Illingworth, G. D. 2008, *ApJ*, 682, 896, doi: [10.1086/589677](https://doi.org/10.1086/589677)
- Kriek, M., van Dokkum, P. G., Labbé, I., et al. 2009, *ApJ*, 700, 221, doi: [10.1088/0004-637X/700/1/221](https://doi.org/10.1088/0004-637X/700/1/221)
- Kriek, M., van Dokkum, P. G., Franx, M., et al. 2006, *ApJL*, 649, L71, doi: [10.1086/508371](https://doi.org/10.1086/508371)
- Kriek, M., Conroy, C., van Dokkum, P. G., et al. 2016, *Nature*, 540, 248, doi: [10.1038/nature20570](https://doi.org/10.1038/nature20570)
- Kriek, M., Price, S. H., Conroy, C., et al. 2019, *ApJL*, 880, L31, doi: [10.3847/2041-8213/ab2e75](https://doi.org/10.3847/2041-8213/ab2e75)
- Kroupa, P. 2001, *MNRAS*, 322, 231, doi: [10.1046/j.1365-8711.2001.04022.x](https://doi.org/10.1046/j.1365-8711.2001.04022.x)
- Kroupa, P., & Boily, C. M. 2002, *MNRAS*, 336, 1188, doi: [10.1046/j.1365-8711.2002.05848.x](https://doi.org/10.1046/j.1365-8711.2002.05848.x)
- Lawlor-Forsyth, C., Balogh, M. L., Sazonova, E., et al. 2026, *ApJ*, 1000, 61, doi: [10.3847/1538-4357/ae4502](https://doi.org/10.3847/1538-4357/ae4502)
- Leja, J., Carnall, A. C., Johnson, B. D., Conroy, C., & Speagle, J. S. 2019, *ApJ*, 876, 3, doi: [10.3847/1538-4357/ab133c](https://doi.org/10.3847/1538-4357/ab133c)
- Leung, H.-H., Wild, V., Papatthomas, M., et al. 2024, *MNRAS*, 528, 4029, doi: [10.1093/mnras/stae225](https://doi.org/10.1093/mnras/stae225)
- Leung, H.-H., Wild, V., Papatthomas, M., Carnall, A. C., & Chen, Y. 2025, *MNRAS*, 543, 738, doi: [10.1093/mnras/staf1493](https://doi.org/10.1093/mnras/staf1493)
- Leung, H.-H., Carnall, A. C., Taylor, E., et al. 2026a, arXiv e-prints, arXiv:2602.05934, doi: [10.48550/arXiv.2602.05934](https://doi.org/10.48550/arXiv.2602.05934)
- Leung, H.-H., Wild, V., Papatthomas, M., et al. 2026b, arXiv e-prints, arXiv:2602.13114, <https://arxiv.org/abs/2602.13114>
- Lisiecki, K., Donevski, D., Man, A. W. S., et al. 2026, *A&A*, 708, A235, doi: [10.1051/0004-6361/202557118](https://doi.org/10.1051/0004-6361/202557118)
- Looser, T. J., D'Eugenio, F., Maiolino, R., et al. 2024, *Nature*, 629, 53, doi: [10.1038/s41586-024-07227-0](https://doi.org/10.1038/s41586-024-07227-0)
- Lovell, C. C., Harrison, I., Harikane, Y., Tacchella, S., & Wilkins, S. M. 2023, *MNRAS*, 518, 2511, doi: [10.1093/mnras/stac3224](https://doi.org/10.1093/mnras/stac3224)
- Maiolino, R., & Mannucci, F. 2019, *A&A Rv*, 27, 3, doi: [10.1007/s00159-018-0112-2](https://doi.org/10.1007/s00159-018-0112-2)
- Man, A. W. S., Toft, S., Zirm, A. W., Wuyts, S., & van der Wel, A. 2012, *ApJ*, 744, 85, doi: [10.1088/0004-637X/744/2/85](https://doi.org/10.1088/0004-637X/744/2/85)
- Maoz, D., & Gal-Yam, A. 2004, *MNRAS*, 347, 951, doi: [10.1111/j.1365-2966.2004.07232.x](https://doi.org/10.1111/j.1365-2966.2004.07232.x)

- Maoz, D., Sharon, K., & Gal-Yam, A. 2010, *ApJ*, 722, 1879, doi: [10.1088/0004-637X/722/2/1879](https://doi.org/10.1088/0004-637X/722/2/1879)
- Marchesini, D., Whitaker, K. E., Brammer, G., et al. 2010, *ApJ*, 725, 1277, doi: [10.1088/0004-637X/725/1/1277](https://doi.org/10.1088/0004-637X/725/1/1277)
- Marchesini, D., Muzzin, A., Stefanon, M., et al. 2014, *ApJ*, 794, 65, doi: [10.1088/0004-637X/794/1/65](https://doi.org/10.1088/0004-637X/794/1/65)
- Marsan, Z. C., Marchesini, D., Brammer, G. B., et al. 2017, *ApJ*, 842, 21, doi: [10.3847/1538-4357/aa7206](https://doi.org/10.3847/1538-4357/aa7206)
- McClymont, W., Tacchella, S., Smith, A., et al. 2025, *MNRAS*, 544, 1732, doi: [10.1093/mnras/staf1861](https://doi.org/10.1093/mnras/staf1861)
- McConachie, I., Antwi-Danso, J., Chang, W., et al. 2025a, arXiv e-prints, arXiv:2508.05752, doi: [10.48550/arXiv.2508.05752](https://doi.org/10.48550/arXiv.2508.05752)
- McConachie, I., de Graaff, A., Maseda, M. V., et al. 2025b, arXiv e-prints, arXiv:2510.25024, doi: [10.48550/arXiv.2510.25024](https://doi.org/10.48550/arXiv.2510.25024)
- McDonough, B., Curtis, O., & Brainerd, T. G. 2025, *ApJ*, 978, 67, doi: [10.3847/1538-4357/ad9747](https://doi.org/10.3847/1538-4357/ad9747)
- Mosleh, M., Tacchella, S., Renzini, A., et al. 2017, *ApJ*, 837, 2, doi: [10.3847/1538-4357/aa5f14](https://doi.org/10.3847/1538-4357/aa5f14)
- Muzzin, A., Labbé, I., Franx, M., et al. 2012, *ApJ*, 761, 142, doi: [10.1088/0004-637X/761/2/142](https://doi.org/10.1088/0004-637X/761/2/142)
- Muzzin, A., Marchesini, D., Stefanon, M., et al. 2013, *ApJ*, 777, 18, doi: [10.1088/0004-637X/777/1/18](https://doi.org/10.1088/0004-637X/777/1/18)
- Muzzin, A., van der Burg, R. F. J., McGee, S. L., et al. 2014, *ApJ*, 796, 65, doi: [10.1088/0004-637X/796/1/65](https://doi.org/10.1088/0004-637X/796/1/65)
- Nanayakkara, T., Glazebrook, K., Jacobs, C., et al. 2024, *Scientific Reports*, 14, 3724, doi: [10.1038/s41598-024-52585-4](https://doi.org/10.1038/s41598-024-52585-4)
- Nelson, E. J., van Dokkum, P. G., Förster Schreiber, N. M., et al. 2016, *ApJ*, 828, 27, doi: [10.3847/0004-637X/828/1/27](https://doi.org/10.3847/0004-637X/828/1/27)
- Newman, A. B., Belli, S., & Ellis, R. S. 2015, *ApJL*, 813, L7, doi: [10.1088/2041-8205/813/1/L7](https://doi.org/10.1088/2041-8205/813/1/L7)
- Newman, A. B., Belli, S., Ellis, R. S., & Patel, S. G. 2018, *ApJ*, 862, 126, doi: [10.3847/1538-4357/aacd4f](https://doi.org/10.3847/1538-4357/aacd4f)
- Newman, A. B., Ellis, R. S., Treu, T., & Bundy, K. 2010, *ApJL*, 717, L103, doi: [10.1088/2041-8205/717/2/L103](https://doi.org/10.1088/2041-8205/717/2/L103)
- Ni, Y., Chen, N., Zhou, Y., et al. 2025, *ApJ*, 990, 120, doi: [10.3847/1538-4357/adf3a7](https://doi.org/10.3847/1538-4357/adf3a7)
- Oldham, L., Auger, M., Fassnacht, C. D., et al. 2017, *MNRAS*, 470, 3497, doi: [10.1093/mnras/stx1127](https://doi.org/10.1093/mnras/stx1127)
- Oser, L., Ostriker, J. P., Naab, T., Johansson, P. H., & Burkert, A. 2010, *ApJ*, 725, 2312, doi: [10.1088/0004-637X/725/2/2312](https://doi.org/10.1088/0004-637X/725/2/2312)
- Palakkatharappil, D. B., & Creevey, O. L. 2023, *A&A*, 674, A146, doi: [10.1051/0004-6361/202243624](https://doi.org/10.1051/0004-6361/202243624)
- Park, M., Conroy, C., Johnson, B. D., et al. 2025, *ApJ*, 994, 165, doi: [10.3847/1538-4357/ae0cba](https://doi.org/10.3847/1538-4357/ae0cba)
- Park, M., Belli, S., Conroy, C., et al. 2023, *ApJ*, 953, 119, doi: [10.3847/1538-4357/acd54a](https://doi.org/10.3847/1538-4357/acd54a)
- Park, M., Belli, S., Conroy, C., et al. 2024, *ApJ*, 976, 72, doi: [10.3847/1538-4357/ad7e15](https://doi.org/10.3847/1538-4357/ad7e15)
- Pathak, D., Belli, S., & Weinberger, R. 2021, *ApJL*, 916, L23, doi: [10.3847/2041-8213/ac13a7](https://doi.org/10.3847/2041-8213/ac13a7)
- Pérez-González, P. G., D'Eugenio, F., Rodríguez del Pino, B., et al. 2025, *Nature Astronomy*, doi: [10.1038/s41550-025-02586-8](https://doi.org/10.1038/s41550-025-02586-8)
- Pietrinferni, A., Cassisi, S., Salaris, M., & Castelli, F. 2004, *ApJ*, 612, 168, doi: [10.1086/422498](https://doi.org/10.1086/422498)
- Pietrinferni, A., Cassisi, S., Salaris, M., & Castelli, F. 2006, *ApJ*, 642, 797, doi: [10.1086/501344](https://doi.org/10.1086/501344)
- Pipino, A., & Matteucci, F. 2009, in *IAU Symposium*, Vol. 258, *The Ages of Stars*, ed. E. E. Mamajek, D. R. Soderblom, & R. F. G. Wyse, 39–50, doi: [10.1017/S174392130903169X](https://doi.org/10.1017/S174392130903169X)
- Pizzardo, M., Damjanov, I., Sohn, J., & Geller, M. J. 2026, *A&A*, 705, A30, doi: [10.1051/0004-6361/202556368](https://doi.org/10.1051/0004-6361/202556368)
- Salpeter, E. E. 1955, *ApJ*, 121, 161, doi: [10.1086/145971](https://doi.org/10.1086/145971)
- Sánchez-Blázquez, P., Peletier, R. F., Jiménez-Vicente, J., et al. 2006, *MNRAS*, 371, 703, doi: [10.1111/j.1365-2966.2006.10699.x](https://doi.org/10.1111/j.1365-2966.2006.10699.x)
- Schaefer, A. L., Croom, S. M., Allen, J. T., et al. 2017, *MNRAS*, 464, 121, doi: [10.1093/mnras/stw2289](https://doi.org/10.1093/mnras/stw2289)
- Schreiber, C., Glazebrook, K., Nanayakkara, T., et al. 2018, *A&A*, 618, A85, doi: [10.1051/0004-6361/201833070](https://doi.org/10.1051/0004-6361/201833070)
- Schwarz, G. 1978, *Annals of Statistics*, 6, 461
- Setton, D. J., Bezanson, R., Suess, K. A., et al. 2020, *ApJ*, 905, 79, doi: [10.3847/1538-4357/abc265](https://doi.org/10.3847/1538-4357/abc265)
- Skarbinski, M., Rowlands, K., Alatalo, K., et al. 2026, *ApJ*, 1000, 191, doi: [10.3847/1538-4357/ae459d](https://doi.org/10.3847/1538-4357/ae459d)
- Skipper, S., & Josef, P. 2010, 9th Python in Science Conference
- Slob, M., Kriek, M., Beverage, A. G., et al. 2024, *ApJ*, 973, 131, doi: [10.3847/1538-4357/ad65ff](https://doi.org/10.3847/1538-4357/ad65ff)
- Smolčić, V., Karim, A., Miettinen, O., et al. 2015, *A&A*, 576, A127, doi: [10.1051/0004-6361/201424996](https://doi.org/10.1051/0004-6361/201424996)
- Straatman, C. M. S., Labbé, I., Spitler, L. R., et al. 2014, *ApJL*, 783, L14, doi: [10.1088/2041-8205/783/1/L14](https://doi.org/10.1088/2041-8205/783/1/L14)
- Straatman, C. M. S., van der Wel, A., Bezanson, R., et al. 2018, *ApJS*, 239, 27, doi: [10.3847/1538-4365/aac37a](https://doi.org/10.3847/1538-4365/aac37a)
- Suess, K. A., Kriek, M., Price, S. H., & Barro, G. 2020, *ApJL*, 899, L26, doi: [10.3847/2041-8213/abacc9](https://doi.org/10.3847/2041-8213/abacc9)
- Takahashi, K., Morishita, T., Kodama, T., et al. 2025, arXiv e-prints, arXiv:2505.05942, doi: [10.48550/arXiv.2505.05942](https://doi.org/10.48550/arXiv.2505.05942)
- Thomas, D., Maraston, C., Bender, R., & Mendes de Oliveira, C. 2005, *ApJ*, 621, 673, doi: [10.1086/426932](https://doi.org/10.1086/426932)

- Toft, S., Smolčić, V., Magnelli, B., et al. 2014, *ApJ*, 782, 68, doi: [10.1088/0004-637X/782/2/68](https://doi.org/10.1088/0004-637X/782/2/68)
- Urbano Stawinski, S. M., Cooper, M. C., Forrest, B., et al. 2024, *The Open Journal of Astrophysics*, 7, 46, doi: [10.33232/001c.120087](https://doi.org/10.33232/001c.120087)
- Valentino, F., Tanaka, M., Davidzon, I., et al. 2020, *ApJ*, 889, 93, doi: [10.3847/1538-4357/ab64dc](https://doi.org/10.3847/1538-4357/ab64dc)
- van de Sande, J., Kriek, M., Franx, M., et al. 2013, *ApJ*, 771, 85, doi: [10.1088/0004-637X/771/2/85](https://doi.org/10.1088/0004-637X/771/2/85)
- van der Wel, A., Noeske, K., Bezanson, R., et al. 2016, *ApJS*, 223, 29, doi: [10.3847/0067-0049/223/2/29](https://doi.org/10.3847/0067-0049/223/2/29)
- van der Wel, A., Bezanson, R., D'Eugenio, F., et al. 2021, *ApJS*, 256, 44, doi: [10.3847/1538-4365/ac1356](https://doi.org/10.3847/1538-4365/ac1356)
- van Dokkum, P. G., & Franx, M. 2001, *ApJ*, 553, 90, doi: [10.1086/320645](https://doi.org/10.1086/320645)
- van Dokkum, P. G., Franx, M., Kriek, M., et al. 2008, *ApJL*, 677, L5, doi: [10.1086/587874](https://doi.org/10.1086/587874)
- van Dokkum, P. G., Whitaker, K. E., Brammer, G., et al. 2010, *ApJ*, 709, 1018, doi: [10.1088/0004-637X/709/2/1018](https://doi.org/10.1088/0004-637X/709/2/1018)
- Vazdekis, A., Coelho, P., Cassisi, S., et al. 2015, *MNRAS*, 449, 1177, doi: [10.1093/mnras/stv151](https://doi.org/10.1093/mnras/stv151)
- Villaume, A., Conroy, C., Johnson, B., et al. 2017, *ApJS*, 230, 23, doi: [10.3847/1538-4365/aa72ed](https://doi.org/10.3847/1538-4365/aa72ed)
- Walters, D., Woo, J., & Ellison, S. L. 2022, *MNRAS*, 511, 6126, doi: [10.1093/mnras/stac283](https://doi.org/10.1093/mnras/stac283)
- Webb, K. A., Villaume, A., Laine, S., et al. 2022, *MNRAS*, 516, 3318, doi: [10.1093/mnras/stac2417](https://doi.org/10.1093/mnras/stac2417)
- Weibel, A., de Graaff, A., Setton, D. J., et al. 2025, *ApJ*, 983, 11, doi: [10.3847/1538-4357/adab7a](https://doi.org/10.3847/1538-4357/adab7a)
- Whitaker, K. E., van Dokkum, P. G., Brammer, G., et al. 2013, *ApJL*, 770, L39, doi: [10.1088/2041-8205/770/2/L39](https://doi.org/10.1088/2041-8205/770/2/L39)
- Wilkinson, A., Almaini, O., Chen, C.-C., et al. 2017, *MNRAS*, 464, 1380, doi: [10.1093/mnras/stw2405](https://doi.org/10.1093/mnras/stw2405)
- Wright, L., Whitaker, K. E., Weaver, J. R., et al. 2024, *ApJL*, 964, L10, doi: [10.3847/2041-8213/ad2b6d](https://doi.org/10.3847/2041-8213/ad2b6d)
- Wu, P.-F., van der Wel, A., Bezanson, R., et al. 2020, *ApJ*, 888, 77, doi: [10.3847/1538-4357/ab5fd9](https://doi.org/10.3847/1538-4357/ab5fd9)
- Yang, T., Wang, T., Xu, K., et al. 2026, *ApJL*, 1000, L42, doi: [10.3847/2041-8213/ae4803](https://doi.org/10.3847/2041-8213/ae4803)
- Zavala, J. A., Faisst, A. L., Aravena, M., et al. 2026, *ApJL*, 998, L36, doi: [10.3847/2041-8213/ae382a](https://doi.org/10.3847/2041-8213/ae382a)
- Zewdie, D., Pović, M., Aravena, M., Assef, R. J., & Gaulle, A. 2020, *MNRAS*, 498, 4345, doi: [10.1093/mnras/staa2488](https://doi.org/10.1093/mnras/staa2488)
- Zhang, Y., de Graaff, A., Setton, D. J., et al. 2026a, *ApJ*, 997, 252, doi: [10.3847/1538-4357/ae24e1](https://doi.org/10.3847/1538-4357/ae24e1)
- Zhang, Y., Ji, Z., Bezanson, R., et al. 2026b, *arXiv e-prints*, arXiv:2604.05024, doi: [10.48550/arXiv.2604.05024](https://doi.org/10.48550/arXiv.2604.05024)